Master *Radiation and its Effects on MicroElectronics and PhotonicsTechnologies* (RADMEP)

When Fringe Meets Finesse: Compact Iodine-Stabilized Lasers in Two-Colour Length Interferometry

Master Thesis Report

Presented by

Rubén Enrique Montero Franco

and defended at

University Jean Monnet

11/09/2023

Academic Supervisor(s): Dr. Arto Javanainen

Prof. Sylvain Girard

Host Supervisor: Dr. Antti Lassila

Jury Committee: Dr. Arto Javanainen, University of Jyväskylä

Prof. Sylvain Girard, University Jean Monnet

Prof. Paul Leroux, Catholic University of Leuven

Prof. Frédéric Saigné, University of Montpellier

Abstract

This master's thesis focuses on developing a feedback loop system for stabilizing semiconductor lasers to low-pressure iodine gas absorption spectra. The goal is to generate stable wavelengths at $531\,nm$ and $688\,nm$, essential for precise two-colour length measurement interferometry in laboratories.

Semiconductor lasers are versatile light sources with broad applications in telecommunications and scientific instrumentation. However, for accurate length measurement interferometry, a stable wavelength source is vital. The thesis proposes a feedback loop system that achieves relative frequency stability levels of 10^{-9} by utilizing low-pressure iodine gas absorption spectra to stabilize the lasers.

The research involves creating a compact device using commercially available diode lasers and short iodine cells, resulting in a footprint of $15\,cm\,x\,15\,cm\,x\,10\,cm$. Experimental evaluations demonstrate an uncertainty of $3\,MHz$, a relative frequency stability in the order of 10^{-9} for both the green and red lasers with an Allan deviation in the order of 10^{-10} and 10^{-9} for the green and red lasers, respectively, making the system suitable for practical applications, including gauge block measurements.

This work contributes to the advancement of two-colour length measurement interferometry by providing a compact and stable wavelength generation system. The research opens up possibilities for enhanced accuracy and reliability in scientific and industrial applications.

Table of Contents

Acknowledgements

I want to express my heartfelt gratitude for the guidance and unwavering support I received during the completion of this thesis. I am immensely thankful to my supervisors at VTT, Dr. Jeremias Seppä and Dr. Antti Lassila, who played a crucial role in shaping this work with their valuable insights and endless patience. Their dedication to excellence motivated me to delve deeper into the subject, and I sincerely appreciate their confidence in my abilities.

I feel incredibly fortunate to have had Dr. Arto Javanainen from the University of Jyväskylä and Prof. Sylvain Girard from Jean Monnet University as my supervisors. Their extensive knowledge and clear direction kept me on track throughout the research. Their constructive criticism and insightful feedback significantly contributed to improving the final output.

I am grateful for the supportive and conducive environment provided by both RADMEP and VTT Technical Research Centre of Finland Ltd, which was instrumental in the successful completion of my master's thesis.

Lastly, I want to convey my deepest appreciation to my family for their unwavering support and belief in me. Their encouragement has been a constant source of motivation throughout this academic journey. Furthermore, I also want to express my appreciation to my friends, particularly to Stefano, for his patience and helping me understand a bit better microelectronics, to Theresa, for her confidence and her craziness, to Cashmere, for being there in the difficult moments, and of course, to Felipe, for everything.

List of Figures

List of Tables

1. Introduction

In recent times, semiconductor lasers have gained prominence as highly adaptable light sources, finding extensive utility across various domains such as telecommunications and scientific instrumentation. The precise stabilization of the wavelength of these lasers has assumed greater significance, particularly in the context of two-colour length measurement interferometry employed in laboratory environments. This master thesis project sought to address this imperative by devising and executing a feedback loop system for iodine-stabilized semiconductor lasers, operating at $531\,nm$ and $688\,nm$ wavelengths. The primary objective of this work encompassed the development of a relatively compact device capable of generating a stable wavelength conducive to accurate length measurements, complementing the standard $633\,nm$ helium-neon laser, and replacing the $543\,nm$ and $532\,nm$ previously used in the system under development.

1.1 Background and Motivation

The field of semiconductor lasers has seen significant advancements, enabling their widespread use in various scientific and industrial applications. However, for precise length measurement interferometry, a stable and accurately controlled wavelength source is imperative. This is also relevant in situations where measurements at multiple wavelengths are needed, as it enhances the accuracy and reliability of the measurement process.

Optical frequency standards have garnered significant attention across various fields for many years. Recently, advancements have resulted in exceptional accuracies reaching the level of 10^{-18} [1], [2], [3]. Among the earliest and still relevant optical frequency standards are iodine-stabilized lasers, valued for their simplicity and resilience. A specific type, the frequency-doubled Nd:YAG laser, which is stabilized to an iodine absorption line at $532\,nm$, has gained considerable interest due to its remarkable frequency stability [4], [5], [6], [7]. Molecular iodine possesses strong and narrow absorption lines near $532\,nm$, making it ideal for applications utilizing the Nd:YAG laser, such as a flywheel oscillator, an absolute frequency marker for an optical frequency comb, interferometric measurements of gauge blocks, gravitational wave detection, and a laser strainmeter for observing earth tides and earthquakes [8], [9], [10], [11], [12], [13], [14], [15], [16].

For several of these applications, the availability of a compact iodine-stabilized laser emitting in the $531\,nm$ region is highly desirable. Previous experiments have seen the development of compact Nd:YAG systems, with one notable achievement resulting in a laser system measuring $30\,cm \times 45\,cm$ [17]. However, the pursuit of even smaller configurations necessitates the utilization of a small iodine cell and a compact light source. Recent breakthroughs have showcased the potential of an iodine-loaded hollow-core photonic crystal fiber as an alternative to traditional iodine cells [18]. In terms of the light source, a diode laser operating with a wavelength in the vicinity of $531\,nm$ suing a second harmonic generation (SHG) of a $1062\,nm$ distributed-feedback (DFB) laser offers a compact and cost-effective substitute for the Nd:YAG laser. Semiconductor lasers offer usually wider tuning range and simpler control, one temperature and one current, HeNes and Nd:YAGs have more parameters to control. Although diode lasers, such as distributed-feedback (DFB) diode lasers, typically possess broader linewidths exceeding several hundred kilohertz compared to the few kilohertz linewidth of an Nd:YAG laser, diode-laser-based systems may prove suitable for applications that prioritize miniaturization, such as space applications [10], [12], or applications where exceptionally high frequency stability is not an absolute requirement. In this context linewidth refers to the spectral width of the laser's output. It is a measure of the range of frequencies/wavelengths present in the laser beam, lower linewidth values are better for metrology because they lead to improved accuracy, precision, and stability in

measurements. Narrow linewidth lasers provide well-defined reference frequencies or wavelengths that can be relied upon for making highly accurate and consistent measurements.

This thesis introduces a novel approach to address the need for a compact iodine-stabilized laser. For the green laser, emitting at a wavelength of 531 nm, this was achieved by utilizing the technique of second harmonic generation (SHG) with a 1062 nm DFB diode laser, with an output power of 20 mW. For the red laser, we used a coin size discrete mode laser diode emitting at 688 nm, with an output power of 10 mW. The selection of the emission wavelength is based on the availability of commercially available diode lasers operating at these specific frequencies. It is worth mentioning that with the current setup at VTT power is not a critical factor, since most lasers have enough power, from μW to mW.

One of the challenges faced in two-colour length measurement interferometry is the availability of stable wavelength sources that can be easily incorporated into compact devices suitable for laboratory use. Additionally, the requirements for the second wavelength laser suitably far away from the 633 nm wavelength, but still in the visible wavelength range further complicate the development of such devices. Low-pressure iodine gas absorption spectrum offers a reliable and accurate reference for wavelength stabilization. By implementing a feedback loop that accounts for the absorption lines of iodine vapor, it is possible to achieve stability at levels beyond 10^{-8}, which is crucial for precise length measurements, since the relative uncertainty of the laser vacuum wavelength is directly its contribution to the uncertainty budget in the measurement. Typically, with this stability, at 95% confidence the level of uncertainty is 20 nm for short gauge blocks (below 10 mm) and around 100 nm for 1 m gauge blocks. For short gauge blocks the main uncertainty contribution comes from wringing uncertainty and for long gauge blocks uncertainty comes from thermal expansion compensation [19].

To achieve a highly simplified laser system, we adopt a combination of methodologies. Firstly, we leverage on the commercially available coin-sized lasers modules. This integration enhances compactness and ease of implementation. Secondly, we employ a short iodine cell that operates at room temperature, further streamlining the system. Lastly, we stabilize the laser frequency by employing a feedback loop algorithm written in C, that is programmed into a microcontroller (SAML21), this algorithm will tell the microcontroller to drive different temperature and current controllers given the data received from a photodetector [4], [5], [6] [7].

By arranging all the optical components on a 20 $cm \times 30\ cm$ breadboard, we achieve a compact iodine-stabilized laser. However, with further refinement, it is conceivable that the entire setup could be condensed to fit within a volume significantly smaller than $15\ cm \times 15\ cm \times 10\ cm$. These simplifications, although potentially compromising the frequency stability compared to previous Nd:YAG systems [4], [5], [6] [7], pave the way for a highly compact and efficient laser system.

In the experimental evaluation of our compact iodine-stabilized laser, we have achieved remarkable results. Specifically, our lasers system demonstrates an Allan deviation at the level of 10^{-10} and a relative frequency stability at the level of 10^{-9} for the green laser (531 nm). Whereas the red laser 688 nm showed an Allan deviation at the level of 10^{-9} and a relative frequency stability at the level of 10^{-8}, with an uncertainty of $3MHz$ for both devices. These levels of stability prove to be more than sufficient for a wide range of applications, such as laser strainmeter for observing earth tides and earthquakes [8], gravitational wave detection [10], [12], [14], and precise gauge block measurements [16].

The significance of our work lies not only in the development of a compact iodine-stabilized laser operating near the 531 nm and 688 nm wavelengths but also in the novel

approaches employed to simplify the system. By leveraging the advancements in diode laser technology, we have successfully achieved a laser system that meets the demands of various practical applications while significantly reducing its physical footprint.

Moreover, our findings open up new possibilities for further advancements in compact laser systems. As technology continues to evolve, there is potential for the integration of even smaller and more efficient components, leading to further miniaturization and improved performance.

1.2 Two-Colour Length Measurement Interferometry

Considering the utilization of a stabilized laser in conjunction with gauge block measurements through two-colour length measurement interferometry, it becomes essential to elucidate the operational principle underlying this technique. The framework for understanding this method draws inspiration from the content presented in chapter 15 of reference [19]. For a more comprehensive understanding, is recommend referring to the aforementioned chapter.

The establishment of length standards and the capacity to measure length with requisite precision held fundamental significance within any technologically advanced society. Over the course of history, multiple standards for length were developed, initially based on basic human anatomical references such as the cubit and feet. The ongoing enhancement of these standards led to more precise definitions and increasingly accurate techniques for their realization. A notable advancement occurred in 1887 when Michelson proposed the utilization of optical interferometers for length measurement. Nonetheless, it took several years before the meter was officially defined in relation to the wavelength of light emitted by a krypton lamp within a vacuum.

By 1960, this newly established definition replaced the International Prototypes that had been placed in 1889 at the Bureau International des Poids et Mesures (BIPM), where they are still located today. Since 1983, the meter, which stands as one of the seven fundamental units of the International System of Units (SI), has been defined as the distance travelled by light in a vacuum during a time span of 1/299,792,458 of a second.

This definition is rooted in the presence of primary frequency standards, or atomic clocks, that accurately define a second. This definition provides two alternative methods for realizing length measurements:

1) Propagation Delay: The length L represents the distance traversed in a vacuum by a flat electromagnetic wave over a time period t. This relationship is determined by the equation $L = c_0 t$, where c_0 is the speed of light in a vacuum at a value of 299,792,458 meters per second.
2) Interferometry: This approach involves employing the vacuum wavelength λ_0 of a flat electromagnetic wave with a frequency f. This wavelength is derived from the equation $\lambda_0 = c_0 / f$.

The practical implementation of length measurements is contingent on their specific purpose. The propagation delay technique finds its primary utility in scenarios involving significant distances. On the other hand, when it comes to calibrating secondary length standards like gauge blocks, the preferred method is interferometry, utilizing established wavelengths.

The length of these initially calibrated material objects serves as a fundamental bridge between the SI unit of length and its practical applications in both industry and society. This facilitates subsequent mechanical calibrations based on the comparison of length measurements.

The fundamental concept underpinning length measurement through interferometry involves juxtaposing a mechanical length (or spatial distance) with an established light wavelength for comparison. Typically, the optical setup is configured so that the light beam traverses the requisite length twice. Consequently, the units of measurement become half-wavelengths, and the aspired length undergoing measurement is articulated as follows:

$$L = (i + f)\lambda/2$$

where λ is the wavelength, i is the integer order, and f is the fractional order of interference. The concept of representing length in terms of multiples of half-wavelengths is founded on the observation of interference intensities exhibited by two or multiple light waves and is written as:

$$I = I_0\left\{1 + \gamma cos\left[\frac{2\pi}{\lambda/2}(z_1 - z_2)\right]\right\}$$

in the context of two-beam interference, the parameter γ signifies the interference contrast, while $z_1 - z_2$ denotes the disparity in geometric distance along the paths traversed by the two beams. Consequently, modifying the length of one of these pathways results in a periodic alteration of the interference intensity in increments of half the vacuum wavelength $\lambda/2$. The phase difference can be represented using the vacuum wavelength λ_0, indicated as $\frac{2\pi}{\lambda_0/2}n(z_1 - z_2)$. In this context, n denotes the refractive index pertaining to the air within the given path. The expression $n(z_1 - z_2)$ signifies the distinctions between the two optical pathways, rather than disparities between the geometric distances covered.

Visible light typically exhibits wavelengths ranging from 400 to 700 nanometers (nm), resulting in a foundational measurement unit spanning 200 to 350 nm. Through meticulous measurement and analysis of interference patterns (fringes), advanced interferometers can attain measurement uncertainties of less than 1/1000 of a fringe.

Extending the range of wavelengths to even smaller values hold the potential to achieve uncertainties on the order of picometers, particularly in vacuum conditions. However, practical realization encounters persistent constraints, such as challenges related to interferometer alignment. Moreover, new constraints might arise, including the unavailability of suitable monochromatic light sources or complications related to optical components.

One of the most common interferometers use for gauge block measurements is the Twyman-Green interferometer, a variant of the Michelson interferometer, it employs a collimated beam of light. This beam is divided into two separate beams. One of these beams is directed towards a reference mirror, while the other is directed towards an object that is being tested. Each of these beams is reflected and then divided once more at a beam splitter, leading to the occurrence of interference. The resulting pattern of interference, referred to as an "interferogram," is typically observed at the output of the interferometer.

When the object being tested is a flat mirror, and the angles of inclination relative to each incident beam are identical, the entire visual field appears uniformly illuminated. It exhibits a bright appearance in cases where the path difference corresponds to an integral multiple of half the wavelength ($m\lambda/2$), and conversely, appears dark for differences equivalent to half-integral multiples of the wavelength ($(m + ½)\lambda/2$), where m represents an integer.

To conduct measurements of length, a prismatic object, such as a gauge block, can be positioned within the measurement setup, as depicted in Figure 1. The rear surface of the object is connected to a surface referred to as a platen, which serves as a flat mirror,

mirroring the function of the object's front surface. The horizontal displacement of the interference fringes, as illustrated in Figure 1, provides a direct representation of the fractional order of interference. However, determining the integer order of interference becomes impractical due to the presence of interference pattern disruptions caused by the length of the prismatic object.

Undesired secondary reflection originating from the second side of the beam splitter can be mitigated through the application of an antireflection coating. However, even minor remaining reflections can result in disruptive interference patterns. A highly effective solution for eradicating this secondary reflection involves employing a wedge-shaped beam splitter. This configuration alters the direction of the secondary reflection, causing it to deviate from the primary direction. Consequently, the secondary spot formed in the focal plane of the focusing lens can be obstructed using an appropriately sized aperture.

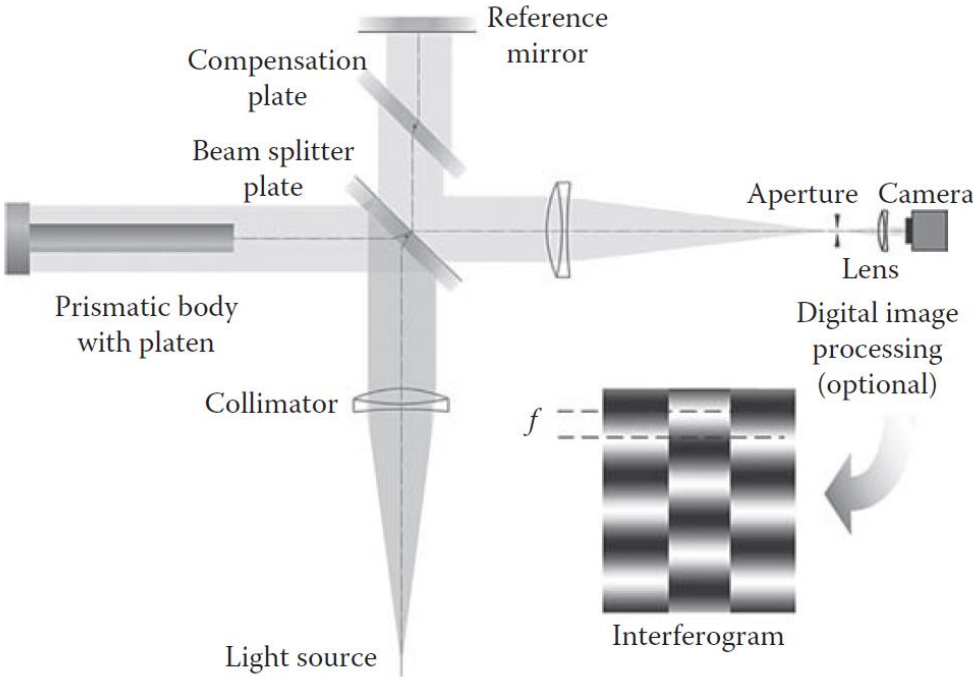

Figure 1: The Twyman-Green interferometer configuration is depicted. A prismatic object is positioned within the path of measurement. To counteract undesired reflections, such as those originating from the rear of the beam splitter, a solution involves employing wedged plates in conjunction with an aperture located at the focal point of the initial output lens. An inset showcases a representative interferogram encompassing both the prismatic body and the platen. This inset serves to illustrate how the visual extraction of the fractional order of interference, denoted as f, can be achieved. Picture taken from [19].

The wedge angle ε of the beam splitter introduces a slight deviation between the interfering beams, calculated as ε times the difference in refractive indices $\varepsilon(n_{BS} - 1)$, where n_{BS} represents the refractive index of the beam splitter. When employing a single wavelength, this deviation is counterbalanced through precise adjustments of the reflecting surfaces. However, due to the dispersion properties of the beam splitter, a substantial variation in the number of observed fringes arises when different wavelengths are utilized.

To address this dispersion effect, a compensatory measure involves inserting a wedge-shaped compensation plate into the reference pathway. The wedge angle, orientation,

and substrate material of this compensation plate must match those of the beam splitter to achieve successful compensation.

In this setup, the reflective surface of the beam splitter is oriented towards the reference mirror. In all other scenarios, while the dispersion effect can potentially be counteracted, it's achievable only when both plates collectively form a parallel configuration. Nonetheless, within this specific arrangement, the influence of the wedge's characteristics itself—particularly the occurrence of an undesired secondary reflection at the beam splitter—is nullified.

When the reference pathway undergoes a shift, any patterns of light and dark bands (fringes) present within the interferogram would exhibit displacement in accordance with the following equation:

$$I = I_0 \left\{1 + \gamma cos\left[\frac{2\pi}{\lambda/2}(z_1 - z_2)\right]\right\}$$

This principle finds application in phase-stepping interferometry, a technique particularly valuable for extensive field Twyman-Green interferometers furnished with camera systems.

In this methodology, multiple interferograms are captured at distinct yet evenly spaced locations along the reference pathway. Using this set of interferograms, algorithms are employed to compute the interference phase distribution at every individual pixel position. Consequently, this procedure enables a more precise determination of the fractional order of interference compared to fringe analysis techniques reliant on single interferograms.

The presence of a monochromatic light source stands as a pivotal factor when applying interferometry for length measurements. Prior to the incorporation of laser radiation into laboratories, generating monochromatic light from alternative sources, such as specialized spectral lamps, posed a significant challenge. While the recommended radiation emissions from spectral lamps for length measurements still endure, these light sources have largely faded into obscurity. In contrast, the list of stabilized laser radiations endorsed by the CIPM (International Committee for Weights and Measures) has steadily expanded over time.

An exemplar of a recommended radiation involves the output of a frequency-doubled Nd:YAG laser, which has been stabilized using an external iodine cell within the laser system. This iodine cell is maintained at a cold-finger temperature of $-15°C$. In this context, the absorbing molecule is $127I_2$, and the specific transition being utilized is the $a10$ component, $R(56)\,32-0$, with a frequency of $563{,}260{,}223{,}513\,kHz$. This corresponds to a vacuum wavelength of $532.245036104\,nm$, and the associated relative standard uncertainty is remarkably low at 8.9×10^{-12}.

This approach not only yields remarkably precise topographical data pertaining to length and height but also imparts insights into the precise lateral alignment of a sample object in relation to the camera array. As a result, this methodology facilitates accurate length measurements even when the object lacks ideal characteristics concerning surface flatness and parallelism.

Using two wavelengths in two colour length measurement interferometry serves the purpose of compensating for the effects of thermal expansion and environmental variations (such as refractive index changes) that can impact precision measurements. Different materials have varying coefficients of thermal expansion, causing their lengths to change with temperature fluctuations. By using two wavelengths, each with different sensitivities to temperature changes, the interferometer can differentiate between actual length changes and those caused by thermal expansion.

Furthermore, when the two wavelengths interact with the gauge block and reference mirror, they produce interference patterns that can be compared. The difference in the interference patterns due to the two colours of light is directly related to the change in length of the gauge block. This differential measurement technique enhances the precision of the measurement.

The separation between the two wavelengths used in a two-colour length measurement interferometer depends on various factors, including the material properties of the gauge block, the desired accuracy of the measurement, and the sensitivity of the interferometer's setup. Generally, a larger separation between the wavelengths provides better compensation for thermal effects, but it may also require more complex optical components.

For most practical applications, the wavelengths are chosen to be far enough apart in the spectrum to ensure distinct sensitivities to temperature changes. A common choice is to use one wavelength in the visible spectrum (e.g., green) and another in the near-infrared spectrum (e.g., red). This choice has several advantages:

Sensitivity Difference: The sensitivity of most materials to temperature changes tends to decrease as you move from the visible to the near-infrared part of the spectrum. This allows for effective compensation of thermal expansion effects.

Optical Components: Many optical components and detectors are readily available for these wavelengths, making it easier to build and calibrate the interferometer.

Measurement Accuracy: A larger separation between the wavelengths improves the accuracy of the compensation for thermal effects.

A typical separation between wavelengths might be around 100 to 200 nanometers or more, depending on the specific interferometer design. However, there is no strict rule, and the choice of separation depends on the specific requirements of the measurement and the interferometer's capabilities.

It's important to also consider factors like the spectral characteristics of the light source, the availability of optical components for the chosen wavelengths, and the interferometer's ability to accurately measure the interference patterns at both wavelengths.

Ultimately, the optimal separation between wavelengths should be determined through careful analysis, experimentation, and possibly simulations to ensure that the chosen wavelengths provide effective thermal compensation and accurate measurements for your specific application.

1.3 Problem Statement

Gauge blocks, introduced by Johansson over a century ago [20], have been instrumental in advancing high precision manufacturing and measurement techniques. These blocks are extensively utilized for calibrating and setting a wide array of measuring instruments, ranging from micrometers and calipers to highly accurate coordinate measuring machines and profilometers. They have been pivotal in establishing manufacturing practices that facilitate interchangeable parts and mass production. Currently, gauge blocks remain one of the most precise transfer standards of length, offering a standard uncertainty of approximately 10 nanometers in central length at their best performance. They hold a critical position in the traceability chains of dimensional measurements across various industries.

Since the inception of gauge blocks, metrologists have been exploring and employing various interferometers for their calibration. These interferometers include the Kösters interferometer [21], NPL Hilger interferometer [22], and Twyman-Green

interferometer [23]. In the early stages, spectral lamps served as light sources, but with the redefinition of the meter in 1983 [24] and the advent of lasers, more accurate wavelength standards became available for interferometry. Initially, phase observation was conducted manually, but the advent of charge-coupled device (CCD) cameras revolutionized fringe recording and analysis, enabling automation [25], [26].

The integration of digital cameras with computers facilitated the adoption of advanced phase analysis techniques, such as phase stepping [27], [28], [29]. Recently, a comprehensive theory encompassing phase stepping has been developed, providing a better understanding of different algorithms and aiding in the selection of appropriate algorithms for specific applications [30], [31]. Through the years, progress in component development and algorithm refinement has significantly enhanced the accuracy and reliability of gauge block metrology, leading to reduced uncertainties in measurements.

Gauge block interferometry needs two single monochromatic stable lasers, there are commercially reasonable price 633 *nm* stabilized laser, but the second laser colour is not economically available. VTT MIKES has provided upgrades to other instruments in these interferometers and has seen that one common problem is that the green laser is not functioning anymore, and is difficult or expensive to repair or replace, in order to be able to provide these updates for gauge block interferometry the development of a secondary laser source is needed.

1.4 Research Objectives

The primary research objectives of this study include:

Implementing a feedback loop with suitable optical and electrical components that stabilizes semiconductor lasers to low-pressure iodine gas absorption spectra.

Developing compact devices capable of generating stable wavelengths at 531 *nm* and 688 *nm* for two-colour length measurement interferometry.

Evaluating the performance of the developed devices and assessing their suitability for laboratory applications.

1.5 Limitations

It is important to acknowledge the limitations that may impact the outcomes of this research, including budget constraints, time limitations, and equipment availability. These factors may influence the extent of the study and the feasibility of certain experimental setups. For instance, one of the main limitations we encounter was the green laser breaking, this was a setback in terms of acquiring new data from this setup. Moreover, the time to get a new green laser was not feasible for this project.

This thesis project aims to contribute to the advancement of two-colour length measurement interferometry by developing compact and stable wavelength generation devices based on semiconductor lasers. By addressing the challenges and limitations, the research endeavours to improve the accuracy and reliability of length measurements in laboratory settings, paving the way for potential applications in diverse scientific and industrial fields.

2. Methodology

This chapter encloses the methods employed to conduct the research in the present master thesis. By providing a comprehensive overview of the research methodology, experimental setup, characterization of the lasers, feedback loop algorithm, data collection methods, data analysis techniques, and obstacles, this study ensured a transparent and rigorous account of the research process. This transparency substantiates the credibility and reliability of the findings, reinforcing the significance and contribution of the present master thesis.

2.1 Research Approach

The device was intended to maintain the same absorption line and stability at laboratory conditions consistently upon activation. The aim was to develop a compact device capable of producing a stable wavelength for use in interferometry, with a relative stability level in the order of 10^{-8}.

An experimental design was employed in this research to enable the manipulation of parameters and evaluate their effects. To accomplish this, an optical test bench was initially set up to characterize the laser and the iodine cell, allowing us to better understand the behaviour of the laser under or laboratory conditions. The microcontroller (SAML21) was tune both digitally, by changing some parameters in the algorithm, and physically, by changing, adding or removing optical components in the optical testbench. This approach allowed for the modification of temperatures, feedback algorithm configurations, and the optical power receive to different measurement devices, such as photodetector (Thorlabs SM1PD1B) and wavelength meter (HighFinesse WS7-30), on the go to assess their effectiveness and precision. This design decision was motivated by the need for accurate measurements and a comprehensive understanding of the causal relationships within the system. The methodology employed in this project drew inspiration from similar approaches documented in references [32], [33], [34].

Data for this study was gathered from multiple sources, including a wavelength meter (HighFinesse WS7-30), a microcontroller (SAML21) connected to a PC, and a photodetector (Thorlabs SM1PD1B). The integration of these data sources resulted in the production of a dataset for analysis. These results were compared to literature values [35]. The validity and dependability of the findings were established through around 40 tests conducted over extended periods of time, ranging from days' worth of data to weeks, depending on the test, ensuring comprehensive data collection and confirmation of consistent results.

In summary, the research methodology employed in this study facilitated a detailed examination of iodine-stabilized lasers operating at wavelengths of 531 *nm* and 688 *nm*. Through meticulous methodological considerations, this study aimed to make insightful contributions to the field of laser stabilization.

2.2 Experimental Setup

The experimental setup employed in this study consisted of a compacted iodine-stabilized diode laser system utilizing saturation absorption. The laser light source was a commercially available diode laser module (QDLASER QLD0593), comprising a DFB diode laser operating at a wavelength of 531 *nm*, a semiconductor optical amplifier (SOA) to amply the distributed feedback signal before conversion, and a periodically poled lithium niobate (PPLN) for second harmonic generation (SHG), all these elements were in the package of the laser.

To measure optical power, a handheld optical power meter was use (Newport 840C) along a Si detector (Newport 818-ST/CM) which had an accuracy of $\pm 0.2\ mW$ in the range of $400 - 1100\ nm$. The $531\ nm$ laser beam with a power of $18.7\ mW \pm 0.2\ mW$ was collimated by an aspheric lens and separated from the fundamental light at 1062 nm using a dichroic mirror (already inside the laser package). The diode laser possessed dimensions of $21.9\ mm \times 5.6\ mm \times 3.8\ mm$ (length × width × thickness), as depicted in Figure 2 a). To facilitate temperature stabilization and control, the module was mounted on two Peltier devices (Micro Peltier Cooler Mocule multicomp pro) and an aluminium block, with dimension of $50\ mm \times 50\ mm \times 10\ mm$ (length × width × thickness), acted as a heatsink.

Temperature control of the laser module was achieved by utilizing a temperature controller (Thorlabs TED200C), which derived the temperature via the two Peltier elements (Micro Peltier Cooler Module multicomp pro), the Peltier elements were place below the laser package, good thermal transfer was procure with the help of thermal paste, under the peltier elements was an aluminium block that acted as a heatsink, see Figure 2 b). The Semiconductor Optical Amplifier (SOA) was driven by a dedicated current controller (Thorlabs LDC202C), while the Distributed Feedback Laser (DFB) was controlled by another current controller (Thorlabs LDC202C).

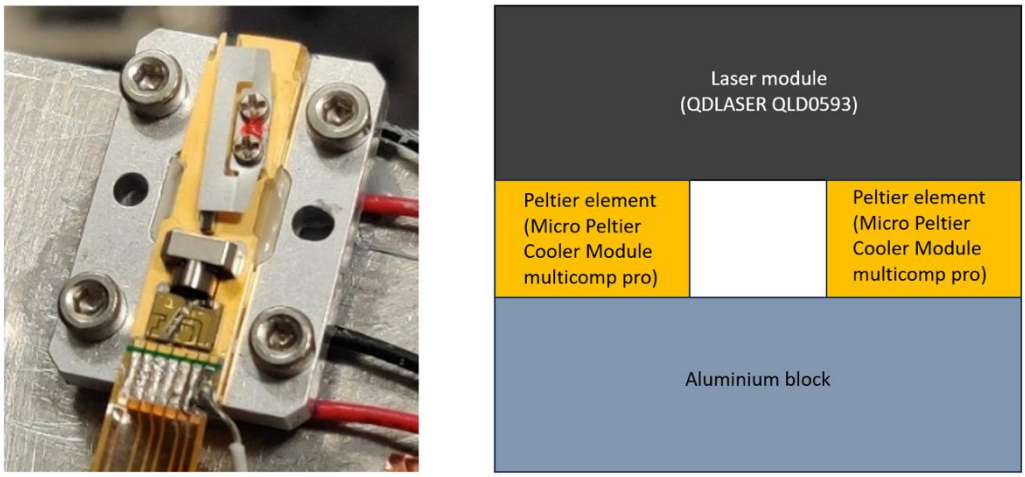

Figure 2: a) Laser Module (QDLASER QLD0593) view from the top. b) parallel view of the mounted laser module, below it two peltier elements (Micro Peltier Cooler Module muticomp pro) for thermal control, and an aluminium block as heatsink, not to scale.

The collimation of the $531\ nm$ laser beam, which had a power output of $19.1\ mW \pm 0.2\ mW$, was achieved using an anti-reflection aspheric lens (Thorlabs CAX100-A). The beam was then reflected with the help of a fused silica broadband dielectric mirror (Thorlabs BB03-E02), this mirror had a coating that only reflected in the range of $400 - 750nm$, according to the manufacturer, this helps us filter any $1062\ nm$ remaining signal. Subsequently, the beam was split in two with a non-polarizing beam splitter (Thorlabs BS035), as shown in Figure 3.

To achieve strong absorption, one path (which had a power of $4.7\ mW \pm 0.2\ mW$) was directed towards a $100\ mm \pm 0.5\ mm$ long iodine cell (Thorlabs GC19100-I), with a cell diameter of $19\ mm \pm 0.5\ mm$, and a purity exceeding 98%. This cell was maintained at a temperature of $19.9°C \pm 0.2°C$, which corresponded to the laboratory temperature, no thermal control was use for the iodine cell. This temperature setting provided adequate absorption strength without necessitating additional heating of the cell. Based on

published iodine vapor pressure data from the manufacturer, the pressure was between $0.1 - 1.2\,Torr$ at $25°C$. The diameter of the beam inside the iodine cell was approximately $1\,mm$.

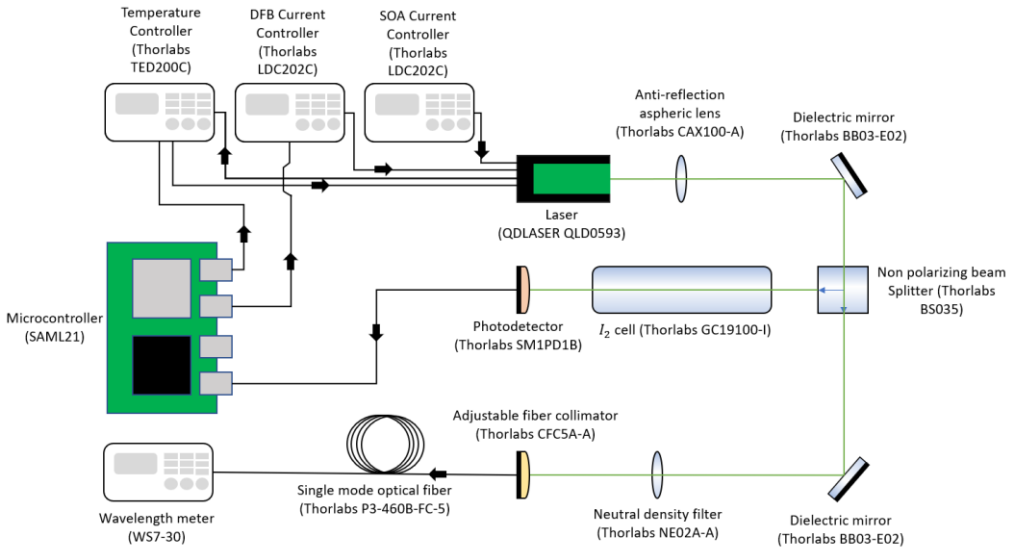

Figure 3: Illustration of the green diode laser setup incorporating a diode laser, mirrors, beam splitter, photodetector, iodine cell, fiber collimator, temperature and current controllers, microcontroller and wavelength meter.

After the iodine cell there was a photodetector (Thorlabs SM1PD1B) to measure the absorption signal, the photodetector was connected to the microcontroller (SAML21) via a BNC coaxial cable (Thorlabs RG-58 BNC Coaxial Cable). The microcontroller (SAML21) is a commercially available Microchip Technology SAM L21 Arm® Cortex®-M0+ Microcontrollers. It has an Arm® Cortex®-M0+ CPU running at up to $48MHz$, with a memory of $128KB$. This microcontroller was already sottered into a PCB designed by VTT MIKES.

The second path, which had a power of $12.2\,mW \pm 0.2\,mW$, was reflected with a fused silica broadband dielectric mirror (Thorlabs BB03-E02) to a neutral density filter (Thorlabs NE02A-A) to reduce the beam intensity, then to the single-mode fiber (Thorlabs P3-460B-FC-5) through an adjustable fiber collimator (Thorlabs CFC5A-A), leading to a high-precision wavelength meter (HighFinesse WS7-30) with an absolute accuracy of $30\,MHz$ ($55\,fm$) and a wavelength deviation sensitivity of $1\,MHz$ ($2\,fm$) in the range of $375 - 800\,nm$ [36].

Throughout the experimental setup, meticulous attention was given to the alignment of all optical elements to ensure optimal quality across the entire optical path. In particular, precautions were taken to prevent reflections back into the iodine cell such as making sure no other beams lead to the cell, using optical elements with anti-reflective coating, thereby minimizing any excessive heating, as well as avoiding any reflection ending up in the detector due to possible artificial etalon effects (an etalon is an optical effect consisting of two partially reflecting surfaces separated by a specific distance, which creates interference patterns due to the multiple reflections of light between these surfaces) in the spectrum. Moreover, all reflections back to the laser were carefully eliminated to avoid disturbances in the DFB, this was particularly addressed with the anti-reflection aspheric lens (Thorlabs CAX100-A).

Additionally, another setup was built using a single-mode laser that operated at a wavelength of 688 nm (Eblana Photonics EP689-0-DM SERIES), with an output power

of 5.9 $mW \pm 0.2\ mW$. The laser had a monolithic design without an external cavity and could be tuned by either temperature or current. It exhibited low sensitivity to mechanical vibration. Similar to the previous setup, temperature control was achieved using a temperature controller (Thorlabs TED200C), which adjusted the temperature through the internal Peltier element (already on the laser package). The distributed feedback (DFB) of the laser was driven by a dedicated current controller (Thorlabs LDC202C).

Consistent with the previous optical setup, meticulous alignment of all optical elements was maintained on the plane of the optical table, ensuring consistent optical quality throughout the entire optical path. In the path containing the iodine cell (Thorlabs GC19100-I), similar measures were taken to prevent reflections back into the iodine cell, as well as any reflections back to the laser to ensure undisturbed operation of the DFB, the beam going to the wavelength meter (HighFinesse WS7-30), had a power of 3.7 $mW \pm 0.2\ mW$ and the beam going to the photodetector (Thorlabs SM1PD1B) had a power of 0.7 $mW \pm 0.2\ mW$

This setup had a lower absorption as compared to the green laser (QDLASER QLD0593). The absorption of iodine in the visible spectrum is due to electronic transitions between its molecular energy levels, and at 688 *nm* we have an absorption of around 9%, the line we choose at 531 *nm* had an absorption of 49%. With the previous optical setup, it was not possible to lock to an iodine absorption line. To account for the reduced absorption exhibited by iodine at the 688 *nm* wavelength, the optical bench for this laser setup included a configuration in which the laser beam passed through the iodine cell twice, this was done with two broadband dielectric mirrors (Thorlabs BB0511-E02) which had a 99% reflectance at this wavelength, see Figure 4. This setup facilitated easier detection of the absorption profile using the photodetector (Thorlabs SM1PD1B), adding the double pass resulted in an absorption of 31%.

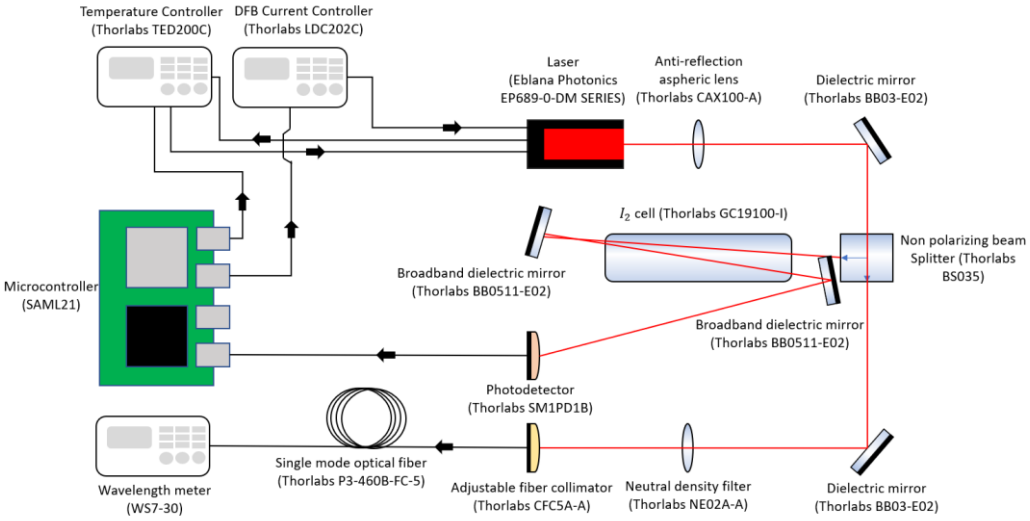

Figure 4: Configuring a red diode laser setup featuring a diode laser, mirrors, beam splitter, photodetector, dual beam pass through an iodine cell, fiber collimator, temperature and current controllers, microcontroller and wavelength meter.

2.3 Characterization of the Lasers

To understand the behaviour of the lasers and the absorption in the iodine cells, the lasers were characterized with the following experiments. This process was conducted to ensure the accuracy and reliability of measurements in this study. To scan the iodine spectrum, the optical frequency of the green diode laser was tuned from

531.632713 $nm \pm 2\ fm$ to 532.239553 $nm \pm 2\ fm$ (393 pm range) by varying the diode temperature from $25 \pm 0.7°C$ to $30 \pm 0.7°C$ (measured using a Fluke 52 k/j thermometer). Two separate runs were performed to obtain a normalized iodine transmission spectrum: one run with the iodine cell (giving us the power values for different absorption lines), and another without it (this run gave us the absolute vales of the power), as presented in Figure 5. Notably, the diode laser exhibited approximately 40 mode hops within this range, as depicted in Figure 6. To visualize both the mode hops and the iodine spectrum, data interpolation was applied, as shown in Figure 7. In contrast, the 688 nm laser could be tuned from 688.350631 $nm \pm 2\ fm$ to 688.650284 $nm \pm 2\ fm$ (300 pm range) without encountering mode hops, this difference in behaviour arises from the difference in the laser, as we are not using the same model, or even manufacturer. This may be due to the difference in cavity length and/or the gain profile of the laser medium.

The mode hopping phenomenon in the green laser (QDLASER QLD0593) is a consequence of the intricate balance between the distributed feedback provided by the grating structure and the gain provided by the active medium within the laser cavity. As the temperature or injection current is adjusted, minute changes in the effective refractive index of the grating altered the resonance condition for different longitudinal modes. This causes the laser to exhibit abrupt and discrete shifts in its dominant emission wavelength, transitioning between different longitudinal modes.

These mode hops manifest themselves as sudden jumps in the output wavelength of the laser. Such shifts can be attributed to the sensitivity of the laser's gain curve to changes in temperature or injection current, and the inherent discrete nature of the grating's effect on feedback. These changes in operating conditions lead to the reordering of longitudinal modes within the laser's gain spectrum, resulting in the observed mode hopping behaviour.

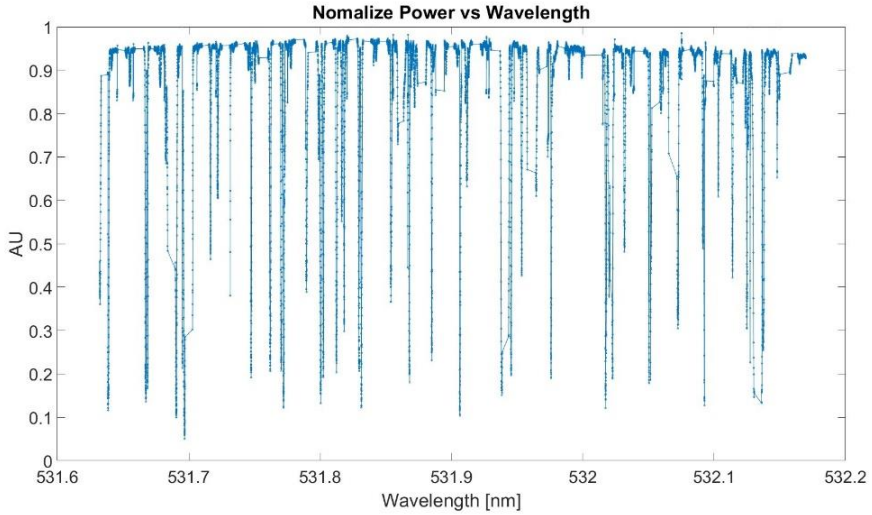

Figure 5: Normalized iodine absorption spectrum showcasing distinct absorption lines within the green laser (QDLASER, QLD0593) range, note that there are lines connecting different absorption lines, this is due to the mode hops.

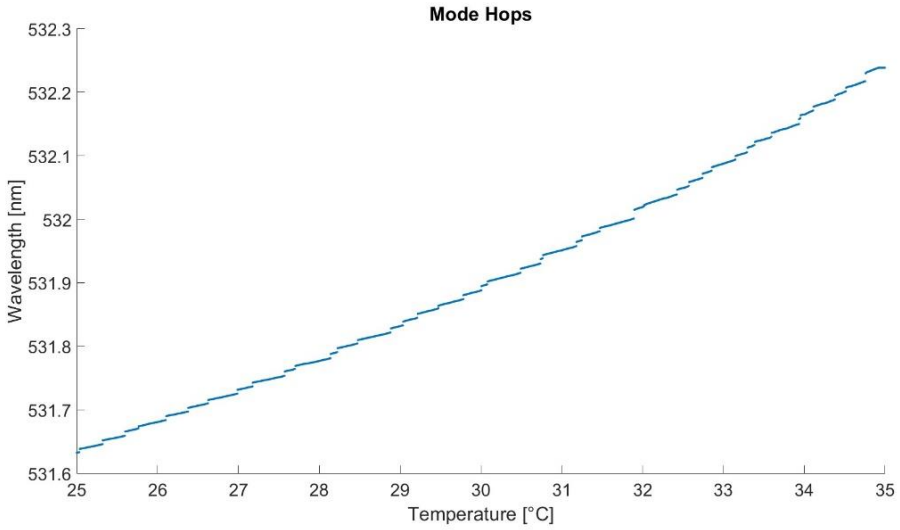

Figure 6: Visualization of mode hops observed in the green laser (QDLASER, QLD0593) range, indicated by wavelength gaps in the plot, representing unavailable emission wavelengths.

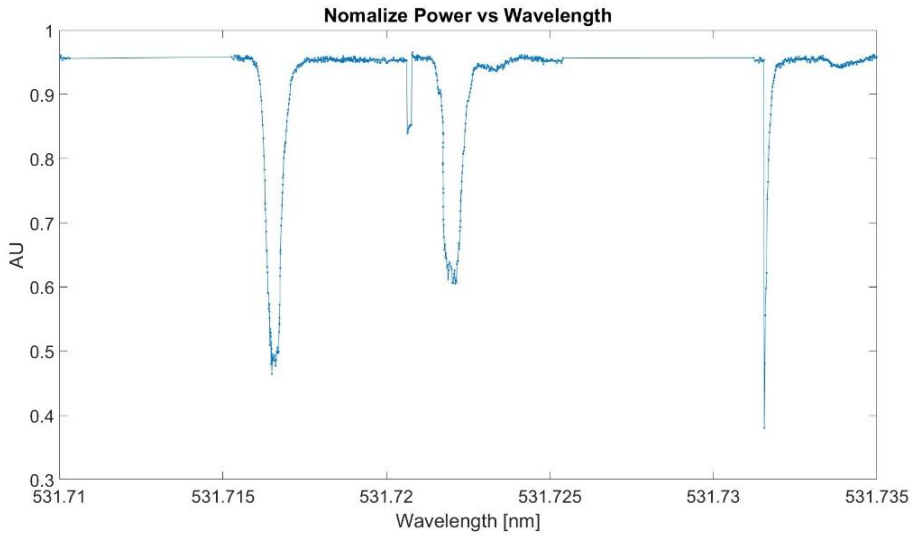

Figure 7: Interpolation between normalized power and wavelength, in the plot we can appreciate two large gaps, these are the mode hops which indicate the absence of certain wavelengths, at least two smaller anomalies (jumps/gaps), two absorption lines and a third one that is being cut by a mode jump (left most peak).

The acquisition system was controlled by a microcontroller (SAML21), which facilitated the connection between the photodetector (Thorlabs SM1PD1B) and the data acquisition process, as illustrated in Figure 3 and Figure 4. We develop a python program to acquire data from the microcontroller (SAML21), including intensity measurements and corresponding timestamps, see Python Acquisition Code.

Concurrently, the microcontroller (SAML21) was programmed in C to send a ramp signal to the temperature controller (Thorlabs TED200C), enabling linear changes in the diode temperature for the purpose of scanning the wavelengths to observe the mode hops and absorption lines. A high-precision wavelength meter ($HighFinesse\ WS7-30$) was utilized during this process to ensure accurate wavelength measurements.

Following the characterization of the laser, an appropriate absorption line meeting specific criteria was selected. These criteria included a sufficient separation from neighbouring absorption lines, minimal proximity to mode hops, and adequate strength for detection within the experimental setup. To identify various spectral lines, reference [35] was consulted.

Once an absorption line was chosen, the region between the two mode hops encompassing the line was determined. This information was crucial for programming the microcontroller to initiate scanning within this region. The selected region was subjected to multiple characterizations at different time points, including immediately after the laser was powered on and after it had been running for several minutes. This ensured that any potential shifts in the mode hops within the spectral region were accounted for.

To achieve laser stabilization on the chosen absorption lines, the green laser (QDLASER, QLD0593) was locked onto the line at $18806.8707 \pm 0.0004\, cm^{-1} = 531.720570 \pm 0.0004\ nm$, while the red laser (Eblana Photonics EP689-0-DM SERIES), exhibiting lower absorption, was locked onto the strongest absorption line within the corresponding range at $14522.6386 \pm 0.0001\, cm^{-1} = 688.580104 \pm 0.0001\, nm$, these values were taken from literature [35].

The microcontroller (SAML21) was programmed to function as a digital feedback loop, initializing the laser stabilization process. By sending a ramp signal to the temperature controller, the microcontroller linearly adjusted the laser temperature to determine the power change corresponding to the absorption of the selected line. Once the desire spectral line is detected, the feedback loop is closed to lock the laser wavelength, a feedback loop was established to maintain stability. This involved modulating the laser wavelength through control of the laser current. Current modulation was chosen due to its capability to provide modulation within the kHz range. Although the impact of laser current on laser frequency was minor (approximately $1\, GHz$ change per $1\, mA$) compared to power variation, it was utilized in the lock to iodine to compensate for rapid fluctuations in laser frequency [37].

To assist with the algorithm tuning process, a Python script was developed to monitor various values from the microcontroller (SAML21), including the error signal and photodetector power. However, it should be noted that directly acquiring data from the microcontroller introduced noise to the system, and therefore, this practice was avoided. The noise appeared in the wavelength measurements as periodical spikes in the data values, this might be due to the microcontroller computational limits since it had only CPU core and running the algorithm that stabilizes the laser while also printing might had apply to much constrain on it. This is not an issue for the overall behaviour of the device, since printing was only needed while tunning the algorithm. To evaluate the stability of the laser, a wavelength meter was employed to assess the performance of the developed device.

2.4 Feedback Loop Algorithm

The feedback loop implemented in C, played a crucial role in stabilizing the laser by effectively utilizing iodine absorption. Its purpose was to continuously adjust the laser's current drive based on the measured input and the desired target value, ensuring that the laser remained stable throughout the operation.

To initiate the process, the code included the necessary libraries and defined constants and variables relevant to the feedback loop. Additionally, it initialized various registers and set up the system for seamless operation. The waveform table constant array was used to store pre-calculated waveform values that were later employed within the feedback loop.

Within the main function, the system was first initialized, and initial values for variables like counters and timers were set. The starting temperature and laser current were also established to provide a solid foundation for the stabilization process.

As the code executed within the main loop, several key actions were carried out. Initially, the generated and mixed values were updated by referencing the waveforms table and the current sine wave index. These values were then utilized to calculate the current drive value using a control factor.

Subsequently, the code examined whether the error signal fell below a specific lock limit threshold. If this condition was met, along with the fulfilment of a time condition, the laser was deemed locked. At this point, the calculated current drive value was assigned to the laser, and a debug print operation was executed periodically to provide valuable insights into the laser stabilization process. This debug print operation showcased pertinent information such as the error signal, input values, and the lock status, aiding in the analysis and monitoring of the stabilization process. As mentioned before, this debug print operation was read using Python, and was the origin of some of the noise introduce to the system.

The code also incorporated temperature scanning logic, which periodically adjusted the temperature based on scan direction and lock status. By updating the temperature variable, which controlled the thermoelectric cooler (TEC) temperature, the code ensured that temperature variations were accounted for and addressed accordingly.

At the end of each iteration, the code introduced a delay and retrieved input from an analog-to-digital converter (ADC) that read the optical power of the laser from a photodetector. The obtained input value was then used to calculate a normalized value, and the sum of the input multiplied by the mixed value was updated accordingly. The sine wave index was incremented, and if it exceeded the size of the waveforms table, it was reset to ensure the proper functioning of the feedback loop. The error signal and error low-pass filter were updated based on the accumulated sum, and the control factor was adjusted accordingly to optimize the stabilization process.

In summary, the code effectively implemented a feedback loop that dynamically adjusted the laser's current drive based on the measured input values, the code also implemented lock-in amplifier and simple (proportional) control. Through continuous comparison between the measured values and the desired target value, the code successfully maintained the stability of the laser system. The incorporation of temperature scanning and locking mechanisms further enhanced the stability and reliability of the system, contributing to the overall success of the laser stabilization process.

2.5 Data Collection

During the characterization of the lasers, a Python code was developed to acquire data from the microcontroller (SAML21), primarily focusing on the photodetector data, but not limited to it. The code was specifically designed for this project, aiming to establish a seamless connection with the microcontroller, retrieve the necessary data, and store it in a well-organized format for subsequent analysis. See Python Acquisition Code for a deeper view into the code itself.

However, it was observed that enabling this data acquisition code when the laser is locked to the spectral line and the laser wavelength is being measured resulted in reduced laser stability. The noise appeared in the wavelength measurements as periodical spikes in the data values, this might be due to the microcontroller (SAML21) computational limits since it had only CPU core and running the algorithm that stabilizes the laser while also printing might had apply to much constrain on it. Consequently, the C code in charge of printing the data within the microcontroller was

disable and the Python code was not use to obtain measurements since continuous data acquisition was not required for the operation of the device.

Instead, highly precise measurements were obtained using a dedicated wavelength meter (HighFinesse WS7-30) with an absolute accuracy of 30 MHz (55 fm) and a wavelength deviation sensitivity of 1 MHz (2 fm) [36]. Despite the high precision capabilities of the device, further analysis revealed potential limitations due to either the meter's resolution or intrinsic noise, or perhaps both factors combined. To investigate this aspect, an iodine-stabilized He-Ne laser locked to the $R(128)11 - 5\ a\ 16\ (f)$ transition, a frequency of 473 612 353 606 802 Hz, and with a stability of 10^{-11} was utilized as a reference, connected to the laboratory's wavelength meter.

2.6 Data Analysis

2.6.1 IQR Method

The stability analysis of the laser system was conducted in this thesis using the IQR (Interquartile Range) method [38], utilizing data obtained from a wavelength meter. Employing this statistical technique provided a robust and comprehensive evaluation of the laser's performance by exploring the dispersion and outliers within the dataset. The utilization of this method was predominantly driven by the intermittent observation of outliers, distinctly attributed to software errors originating from the wavelength meter's (HighFinesse WS7-30) functioning. For instance, while the anticipated values were expected to be within the range of 10^{-9} (nanometers range), occasional instances occurred where values on the scale of 10^{0} surfaced in the dataset, transpiring once or twice every hour of data collection. The employment of this method proved instrumental in effecting the removal of these outliers in a notably more streamlined and efficient manner.

To measure the wavelength emitted by the laser beam over a specific time period, the wavelength meter was employed in this study. The resulting dataset consisted of a series of wavelength measurements, which were subjected to the IQR method to remove any outliers from the dataset [39].

Initially, the dataset was arranged in ascending order to facilitate subsequent calculations. This systematic organization of data allowed for an examination of the distribution and pattern exhibited by the wavelength measurements, aiding in the identification of outliers and providing a clearer understanding of the laser's behaviour.

The application of the IQR method began with the computation of the first quartile ($Q1$), representing the $25th$ percentile of the data. This involved finding the median of the lower half of the dataset, which served as a measure of central tendency. Determining Q1 provided a threshold that defined the lower end of the dataset.

Similarly, the third quartile ($Q3$) was calculated to represent the $75th$ percentile of the data. By finding the median of the upper half of the dataset, $Q3$ established a threshold above which 75% of the wavelength measurements resided, defining the upper end of the dataset.

The interquartile range (IQR) was derived by subtracting $Q1$ from $Q3$, quantifying the spread of the data and serving as a measure of dispersion. Focusing on the middle 50% of the dataset, the IQR method ensured a robust assessment of the laser's stability, as it was less susceptible to the influence of extreme values.

To identify potential outliers within the dataset, a criterion based on the IQR was established. Any wavelength measurement falling below $Q1 - 1.5 * IQR$ or above $Q3 + 1.5 * IQR$ was considered an outlier. These outliers represented values that significantly deviated from the norm, necessitating further investigation. Around 0.3% of the data was consider an outlier.

The presence of outliers could be attributed to various factors, including data entry errors, measurement inaccuracies, or anomalous phenomena. Therefore, it was crucial to individually examine these outliers to determine their validity and assess their impact on the overall analysis.

By employing the IQR method, this study successfully evaluated the stability of the laser based on the wavelength measurements obtained from the wavelength meter. This method offered a reliable measure of dispersion, enabling a thorough exploration of the data and facilitating the identification of outliers, thus enhancing the understanding of the laser's performance characteristics.

It is important to acknowledge that the IQR method is just one of several statistical techniques available for data analysis. Its effectiveness depends on the specific characteristics of the dataset and the objectives of the analysis. Therefore, it is recommended to complement the IQR method with other appropriate statistical techniques to obtain a comprehensive understanding of the laser's stability.

For instance, another known method to remove outliers is the Z-Score method, which calculates the z-score for each data point, it measures how many standard deviations a point is away from the mean. Removing data points with z-scores exceeding a certain threshold, the Z-Score method assumes the data follows a normal distribution, while the IQR method is distribution-agnostic and more suitable for non-normal data. Furthermore, since the data we seek to remove is nine orders of magnitude off one could simply do visualization and manual inspection and remove the data points that are errors. However, this becomes a challenge once the data points go up to the millions, identifying and removing these points becomes non-trivial.

The IQR method proved to be a valuable tool for analysing the stability of the laser system using data from the wavelength meter. Its implementation in this study successfully identified outliers and evaluated the dispersion of the dataset, providing valuable insights into the laser's performance characteristics. The findings from this analysis contribute to a better understanding of the laser's stability and can guide further investigations or improvements in laser technology.

2.6.2 Allan Deviation

When assessing the stability of a frequency standard after its production, it is necessary to conduct tests in order to compare it with other frequency standards. This comparison can be achieved by examining either the phase deviation $\phi(t)$ or the frequency deviation $\Delta\nu(t)$. In order to facilitate comparisons between frequency standards operating at different frequencies, these measures are normalized by dividing them by the nominal frequency.

$$x(t) = \frac{\phi(t)}{2\pi\nu_0}$$

$$y(t) = \frac{\Delta\nu(t)}{\nu_0} = \frac{dx(t)}{dt}$$

The nominal frequency ν_0 serves as a reference value. When analyzing measurements of frequency standards, it is common to use the standard deviation to quantify the variability of the data points by measuring their deviations from the mean value. However, applying this approach to frequency standards presents challenges because the mean value is not always constant, leading to a lack of convergence in the standard deviation.

To address this issue, the Allan deviation is employed, which involves comparing adjacent sets of data points to observe how the data changes over a specific time interval.

This deviation provides insights into the variation of the output frequency standard's measurements.

The standard deviation of a sample can be estimated using the following formula:

$$s = \sqrt{\frac{1}{k-1}\sum_{i=1}^{K}\left(y_i - \frac{1}{K}\sum_{u=i}^{K} y_u\right)^2}$$

In the given equation, K represents the total number of data points, while y_i and y_u denote individual data points. However, to obtain an estimate for the Allan deviation, we will set $K = 2$, resulting in the following expression:

$$s_2 = \frac{1}{2-1}\sum_{i=1}^{2}\left(y_i - \frac{1}{2}\sum_{u=1}^{2} y_u\right)^2 = \frac{1}{2}(y_2 - y_1)^2$$

This approach implies that instead of comparing all values to the mean, we only compare each data point with its neighbouring point. In order to obtain a reliable estimate, this comparison is performed for all data points in the dataset.

$$\sigma_y^2 = \frac{1}{2(M-1)}\sum_{i=1}^{M-1}(y_{i+1} - y_i)$$

Here, M represents the total number of data points, which in the case of the Allan deviation typically corresponds to frequency deviation measurements. The variable σ_y^2 denotes the Allan deviation itself.

Each data point in the dataset is obtained by averaging the measurements over a specific time interval, denoted as τ. The choice of measurement time interval impacts the size of the intervals being compared by the Allan deviation, thereby influencing the calculated value of the deviation. To illustrate the dependence of the Allan deviation on the measurement time, it is common practice to vary τ from a small value to a larger one.

To avoid actually altering the sample time, an alternative approach is employed. It involves taking a series of measurements and progressively increasing the size of the averaged groups of data points. This effectively achieves an increasing τ value without directly changing the measurement time.

To maximize the utilization of the available data and enhance statistical confidence, it is beneficial to calculate the Allan deviation using averaged data with varying offsets. This involves comparing different sets of data points by shifting the comparison window. For example, comparing points $1, 2$, and 3 with points $4, 5$, and 6, and then comparing points $2, 3$, and 4 with points $5, 6$, and 7, and so on. This approach is known as the overlapping Allan deviation and can be expressed by the following equation (refer to [40]):

$$\sigma_y^2 = \frac{1}{2m^2(M-2m+1)}\sum_{i=1}^{M-2m+1}\left(\sum_{u=1}^{j+m-1}(y_{i+m} - y_i\right)^2$$

Performing two nested sums for each τ can become a tedious calculation. However, there is a fortunate simplification when using the phase deviation instead of the frequency deviation, as it eliminates one of the sums in the calculation (refer to [40]):

$$\sigma_y^2 = \frac{1}{(N-2m)} \sum_{i=1}^{N-2m} (y_{i+m} - 2y_{i+m} + y_i)^2$$

In the equation provided, $N = M + 1$ is defined to account for the integration of frequency data to obtain phase data. Integrating the frequency data introduces an additional point, hence the need to adjust the total number of points in the equation (see Figure 8).

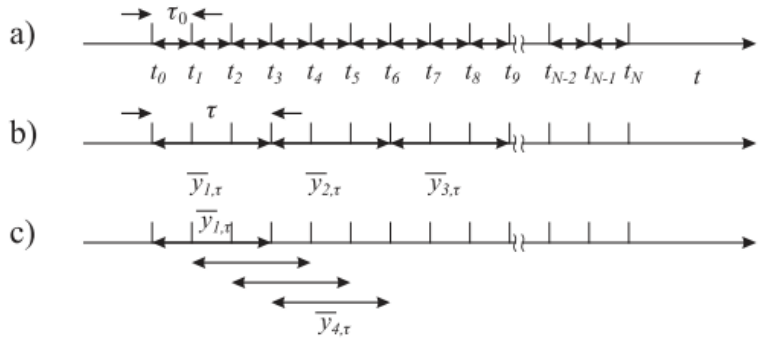

Figure 8: a) Measurements taken at time τ_0. b) are averaged over three data points, resulting in an effective measurement time of $\tau = 3\tau_0$. c) This overlapping averaging technique enhances statistical confidence in the determination of the Allan deviation. Figure taken from [41].

It is important to emphasize that the formulas presented thus far pertain to the estimation of the Allan deviation from a given dataset. The actual Allan deviation is defined as the expectation value of the squared difference, as described in [41]:

$$\sigma_y^2 = \frac{1}{2}(y_2 - y_1)^2$$

Having this understanding allows us to calculate the expected impact of a specific frequency modulation on the Allan deviation. A common scenario is a harmonic modulation, which is highly likely:

$$y(t) = \frac{\Delta\nu}{\nu_0} \sin(2\pi f_m t)$$

Which gives the following Allan deviation (see [40]):

$$\sigma_y(t) = \frac{\Delta\nu}{\nu_0} \frac{\sin^2(2\pi f_m \tau)}{\pi f_m \tau}$$

To delve deeper into this analysis, we can adopt the methodology employed in [42], where the modulation is described in the frequency domain. This approach is advantageous when dealing with complex modulations that may have a simpler representation in the frequency domain compared to the time domain.

Now, the final aspect we need to address regarding the Allan deviation is how to determine the error of our estimate. The subsequent section follows the guidance provided in [43]. In many cases, the phase deviation follows a Gaussian distribution. As the Allan variance is the square of the difference between two y values, it follows a χ^2 distribution. To be more precise, its distribution can be characterized as follows:

$$\chi^2 = \frac{df \cdot \sigma_{ys}^2}{\sigma_{yt}^2}$$

In the equation provided, df represents the degrees of freedom, σ_{ys}^2 corresponds to the Allan variance estimated from the sample, and σ_{yt}^2 denotes the true Allan variance. To determine the minimum and maximum values of the true Allan variance within a given confidence interval, one can examine the distribution of the χ^2 variable.

$$p(\chi^2) = \frac{(\chi^2)^{\frac{df}{2}-1}}{2\ df\ \Gamma\left(\frac{\mathrm{df}}{2}\right)}\ e^{-\frac{x^2}{2}}$$

In the equation provided, Γ represents the gamma function. One notable characteristic of this distribution is that it solely depends on the degrees of freedom. With this knowledge, we can select a desired interval and determine the minimum and maximum values of the χ^2 variable. Once these values are obtained, we can calculate the corresponding minimum and maximum Allan variance.

Determining the degrees of freedom for the case of overlapping Allan deviation can be somewhat intricate, as the overlapping estimates exhibit natural correlations with each other. Additionally, different types of noise introduce varying degrees of data correlation. Thankfully, approximations for the degrees of freedom of overlapping Allan deviation estimates have been developed for different noise types. For the specific noise type present in the system, one can consult the table provided in [40]. This implies that knowing the noise type is crucial for computing the error associated with the Allan deviation.

2.6.3 Error

During the experimental procedure, measurements were conducted while the laser device was situated on a designated test bench. Consequently, inherent discrepancies can be introduced to the setup as a result of minor fluctuations in temperature and humidity levels within the laboratory environment. Additionally, the laser system experienced disruptions caused by slight air currents. To mitigate these issues, the measurements were acquired in an unoccupied laboratory setting.

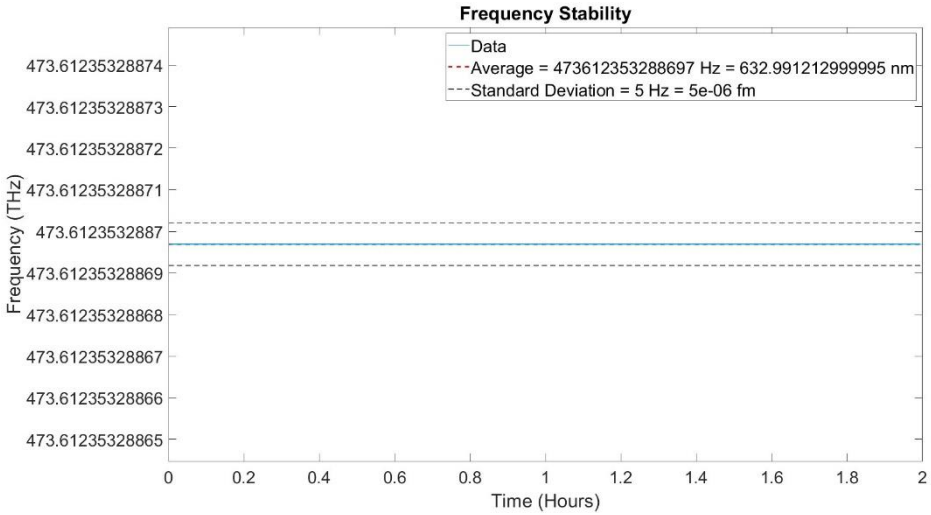

Figure 9: He-Ne laser with a stability of 10^{-11}. *Since the stability of the laser is higher than the sensitivity of the wavelength meter, the plot only shows a straight line.*

Another potential source of error arose from the employment of a specific measurement system, specifically the wavelength meter (HighFinesse WS7-30). This instrument possessed an absolute accuracy of $30MHz\ (55fm)$ and exhibited a sensitivity to

wavelength deviations of $1\,MHz\,(2fm)$ [36]. This indicates that the measured wavelength could deviate by up to 55 fm from the expected value, while being capable of detecting changes in wavelength as minute as 2 fm. To validate this claim, an iodine-stabilized He-Ne laser was utilized, which is reported to have a stability on the order of 10^{-11}. This level of stability surpassed the wavelength meter's detection capabilities, thereby enabling the assumption that the standard deviation of the measurements obtained from the He-Ne laser served as the intrinsic noise inherent to the wavelength. The He-Ne laser was also used to calibrate the wavemeter scale.

Figure 9 illustrates the frequency of the He-Ne laser throughout a duration of 2 hours. Within this time range, the wavelength meter registered a standard deviation of approximately 5 Hz. However, and as discuss in the 2.5 Data Collection subsection, the frequency of the laser is 473 612 353 606 808 Hz, given the stability of the laser, 10^{-11}, is expected that the frequency value is correct up to the 11^{th} digit, 473.61235360 THz. Figure 9 shows that the average frequency is 473 612 353 288 697 Hz, from this is deduced that the wavelength meter is accurate up to the 9^{th} digit, which is in accordance to the accuracy given by the manufacturer [36].

2.7 Challenges

The various challenges, that were encounter during the work and that required careful consideration during data collection and analysis, are listed below.

Equipment Limitations:

One of the primary obstacles we faced was related to the limitations of the equipment used in our experimental setup. Despite our efforts to select high-quality instruments, we encountered constraints such as inherent noise in the equipment as is the case of the microcontroller (SAML21). Furthermore, the green laser broke a few months into the process. While we had already locked and stabilized the laser, it forced us to work with the data we already had.

Environmental Factors:

The research environment itself presented challenges that needed to be addressed. Factors such as temperature fluctuations, vibrations, and electromagnetic interference could influence the stability and performance of the laser system. To mitigate these effects, we implemented measures such as shielding the experimental setup, this mitigated air currents in the vicinity of the laser which help reduce sudden thermal changes and help to mitigate any electromagnetic interference. Maintaining a controlled temperature environment was also crucial while taking data, to approach this, while data was being acquire, the lab was left empty, since most of the thermal variations came from people walking around the setup. However, these factors still posed challenges that had to be carefully considered during data collection and analysis.

Data Integrity and Consistency:

Ensuring the integrity and consistency of the acquired data was another significant obstacle. Due to the complex nature of the experimental setup and data acquisition process, we needed to establish robust protocols and procedures to minimize data loss, artifacts, or inconsistencies. We approached this by repeating the experiment several times, for different periods of time, ensuring that we would lock to the same line each time, and that the stability was maintained.

Time Constraints:

Time constraints-imposed limitations on the scope and extent of our research. Conducting comprehensive experiments and thorough data analysis within the allocated timeframe was a significant challenge. For instance, once the green laser

broke, it was not possible to get a replacement within the timeframe of the thesis, so the project continued with the red laser. However, it is important to acknowledge that additional time could have allowed for more extensive investigations or refined methodologies.

3. Results

3.1 Frequency Stability

Frequency stability measurement was attained through utilization of a wavelength meter, and the resulting data underwent analysis employing the Interquartile Range (IQR) method, as detailed in the 2.6.1 IQR Method subsection, for a detail view of how this method was applied, see the MATLAB Code appendix. Typically, the lasers maintained their locked state for prolonged periods spanning multiple days, even weeks. However, it was observed that over these extended timeframes, the laser's stability was somewhat compromised, albeit without disengaging from the locked state with the iodine absorption line. In order to optimize stability, it was found that the preservation of ideal stability occurred within the temporal domain of hours, this is not an issue for the target application, since such measurements do not take that long. This stability is in parallel to other authors, see [44] and [45]. The novelty in our approach is the compactness of our device, the speed in which it locks (it only takes it a few seconds to stabilized) and the temporal domain in which it stays stable.

3.1.1 Green Laser

Figure 10 shows the achieved stability of the green laser (QDLASER QLD0593) after its successful synchronization with the iodine absorption line. The data was leveled by subtracting the mean frequency from the measure frequency, the data is centered around 0. The laser's average frequency is measured at $563.815665\,THz \pm 1\,MHz$ ($531.720697\,nm \pm 2\,fm$), which closely approximates the literature-reported value of $531.720570\,nm \pm 4\,fm$ [35]. The standard deviation of the laser's frequency is determined to be $3\,MHz$ ($3\,fm$), indicating a relative stability of 5.32×10^{-9}. Notably,

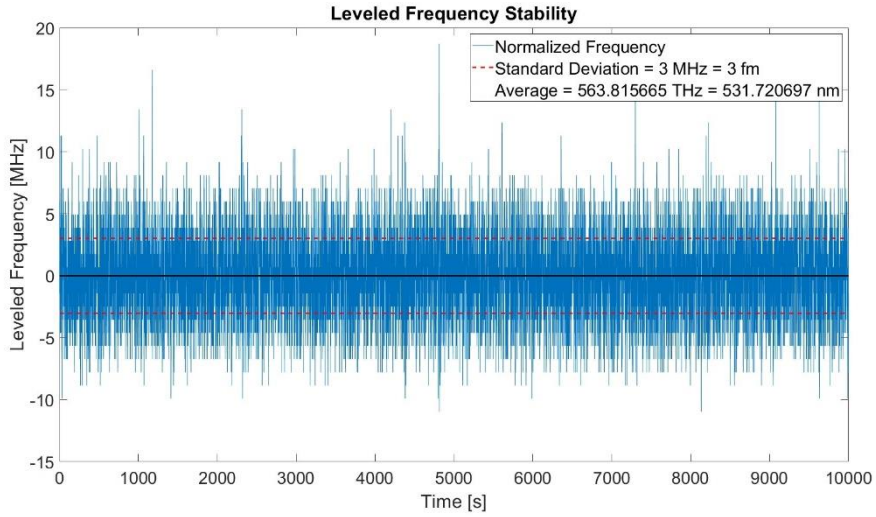

Figure 10: Leveled frequency of the green laser (QDLASER QLD0593) following its successful locking onto the iodine absorption line.

this stability is demonstrated despite the absence of any enclosure for the laser and its vulnerability to external perturbations.

The absolute error can be calculated with the following equation:

$$\text{Absolute Error} = |\text{Experimental Measurement} - \text{Actual Measurement}|$$

$$Absolute\ Error = |531.720697\,nm - 531.720570\,nm| = 1.27 \times 10^{-4}\,nm$$

Relative error is given by:

$$Relative\ Error\ =\ Absolute\ Error/Actual\ Measurement$$

$$Relative\ Error\ =\ 1.27 \times 10^{-4}\ nm\ /\ 531.720570\ nm = 2.38 \times 10^{-7}$$

And finally, we can calculate the percentage error:

$$\text{Percentage Error} = \frac{|\text{Experimental Measurement} - \text{Actual Measurement}|}{\text{Actual Measurement}} \times 100$$

$$Percentage\ Error\ =\ 2.3 \times 10^{-5}\ \%$$

Meaning that there was an 0.000023% error between the measure and literature value. Furthermore, since the standard deviation value of our measurements (3 MHz, 3 fm) was larger than the wavelength meter accuracy (1 MHz, 2 fm) the uncertainty of this setup was 3 MHz (3 fm).

Feature	Value
Measure Average Wavelength	531.720697 $nm\ \pm 2\ fm$
Standard Deviation / Uncertainty	0.000003 $nm\ =\ 3\ fm$
Literature Value Wavelength	531.720570 $nm \pm 4\ fm$
Absolute Error	0.000127 $nm\ =\ 127\ fm$
Relative Error	2.38×10^{-7}
Percentage Error	2.38×10^{-5} %

Table 1: Features and values for the green laser setup.

Figure 11 illustrates the distribution characteristics in the vicinity of the absorption line, revealing that the average value exhibits a higher likelihood of being emitted by the laser when it is in a locked state. The distribution follows a desirable behaviour, adhering to a normal distribution pattern centered around the absorption line.

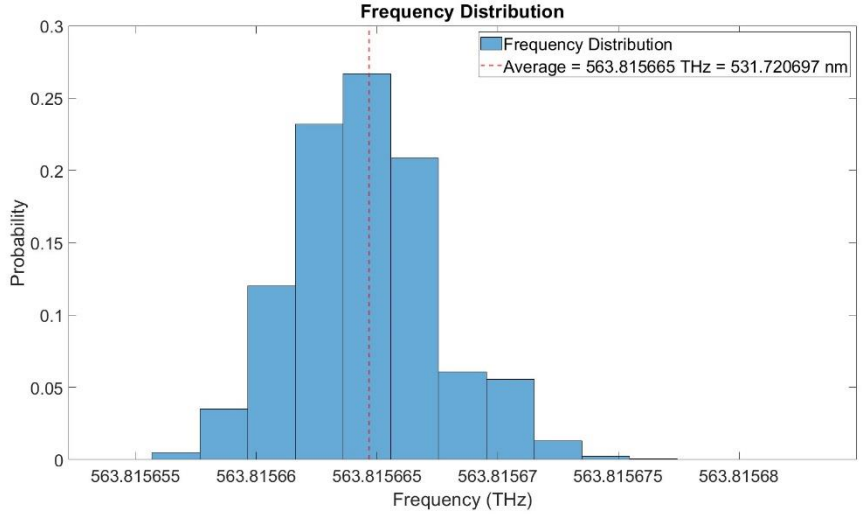

Figure 11: Frequency distribution of the green laser (QDLASER QLD0593) following its successful locking onto the iodine absorption line.

3.1.2 Red Laser

Figure 12 depicts the attained stability of the red laser (Eblana Photonics EP689-0-DM SERIES) subsequent to its successful synchronization with the iodine absorption line. Similar to Figure 10, the data was leveled by subtracting the mean frequency from the measure frequency, the data is centered around 0. The laser's average frequency was quantified at 435.377557 $THz \pm 1MHz$ (688.580413 $nm \pm 2\ fm$), demonstrating a close approximation to the literature-reported value of 688.580104 $nm \pm 1\ fm$ [35].

The standard deviation of the laser's frequency was determined to be 3 MHz (4 fm), indicative of a stability level within the range of 4.36×10^{-9}. This level of stability was notably more challenging to attain in comparison to the stability achieved with the green laser. Various strategies were explored, such as enclosing the experimental setup within a protective box to mitigate the influence of external factors like wind currents and temperature perturbations. However, these efforts did not yield substantial improvements in stability.

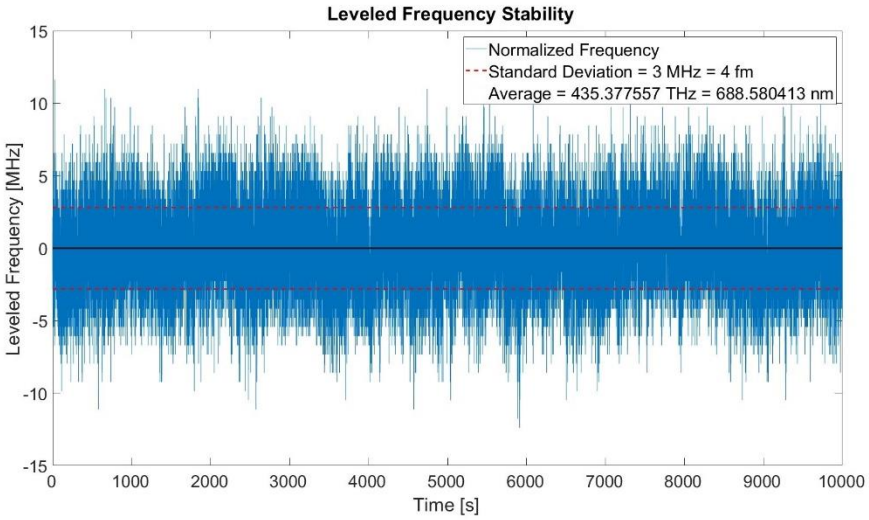

Figure 12: Leveled frequency of the red laser (Eblana Photonics EP689-o-DM SERIES) following its successful locking onto the iodine absorption line.

Ultimately, the key breakthrough that led to a notable improvement in stabilization was achieved through the tuning of the laser's modulation code. By adopting a more aggressive modulation approach for the current controlling the laser, and the desired stability level in the realm of 10^{-9} was successfully realized.

Following a similar procedure as last subsection, we can calculate different features of this setup, see Table 2.

Feature	Value
Measure Average Wavelength	$688.580413\ nm\ \pm\ 2\ fm$
Standard Deviation / Uncertainty	$0.000004\ nm =\ 4\ fm$
Literature Value Wavelength	$688.580104\ nm \pm 1\ fm$
Absolute Error	$0.000309\ nm =\ 309\ fm$
Relative Error	4.48×10^{-7}
Percentage Error	$4.48\ \times 10^{-5}\ \%$

Table 2: Features and values for the red laser setup.

Figure 13 illustrates the distribution characteristics in the vicinity of the absorption line, revealing that the average value exhibits a higher likelihood of being emitted by the laser when it is in a locked state. The distribution follows a desirable behaviour, adhering to a normal distribution pattern centered around the absorption line.

The behavior of the different laser systems was compared by referring to Table 1 and Table 2. In terms of errors, both lasers exhibited an absolute error within a range of a few hundred femtometers, a relative error on the order of 10^{-7}, and a percentage error in the vicinity of 10^{-5}. These measurements aligned well with the values present in existing literature. Additionally, the uncertainty associated with the devices was in the range of a few femtometers ($3fm$ and 4 fm for the green and red lasers, respectively). It's worth noting that the accuracy of the measurements depended on the performance

of the wavelength meter (HighFinesse WS7-30), which provided an accuracy of 2 fm. However, the devices' uncertainties were determined by the standard deviation of the measurements. Since these standard deviations exceeded the accuracy of the wavelength meter, the measurement was not constrained by it. These standard deviation values were thus regarded as indicators of uncertainty. Consequently, it can be asserted that the devices demonstrated precision within a few femtometers and accuracy within a few hundred femtometers.

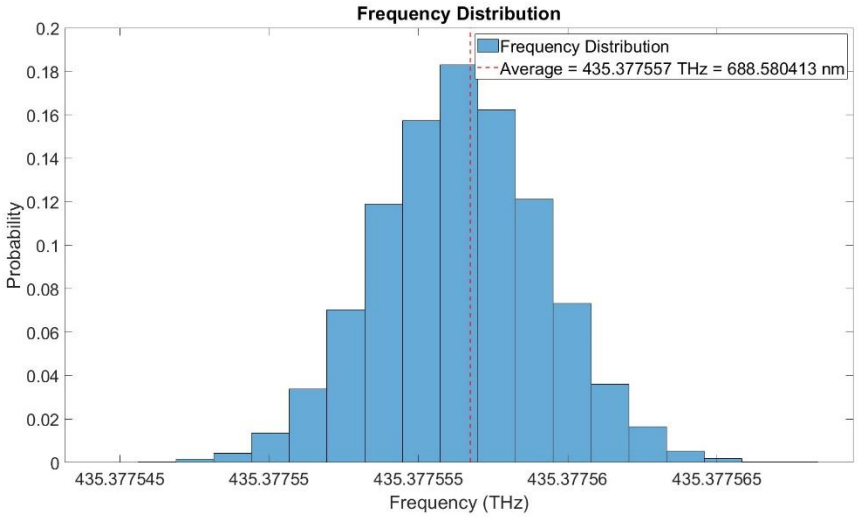

Figure 13: Frequency distribution of the red laser (Eblana Photonics EP689-0-DM SERIES) following its successful locking onto the iodine absorption line.

3.2 Allan Deviation

The Allan Deviation analysis was performed utilizing data acquired from the wavelength meter (HighFinesse WS7-30). The obtained data was subsequently subjected to analysis following the procedure outlined in the Allan Deviation section, a Python code was develop employing the Python library AllanTools version 2019.9 [46], for a detail view see the Allan Calculation Python Code appendix.

For a comprehensive interpretation of such plots, it is beneficial to divide the graph into four distinct regions [40], as illustrated in Figure 14. Each of these regions is elucidated below, and will be mentioned again in more detail for each respective laser:

Point A - In this context, the y-axis value represents the noise associated with an individual measurement point. It characterizes the random fluctuations or variations encountered in each individual measurement.

Point B - By averaging data over time spans along the decreasing slope of the plot, noise that exhibits rapid oscillations can be effectively mitigated. This averaging process aids in correcting the quickly oscillating noise components.

Point C - As the averaging process continues, eventually, a point is reached where the fast-oscillating noise is mostly corrected for. At this minimum point, both the x and y values hold significance and reflect an optimal level of noise correction.

Point D - Subsequently, noise that exhibits oscillations over longer time frames begins to exert an influence on larger groups of average data points. This region signifies the emergence of noise sources with longer-term characteristics that affect the overall measurement data.

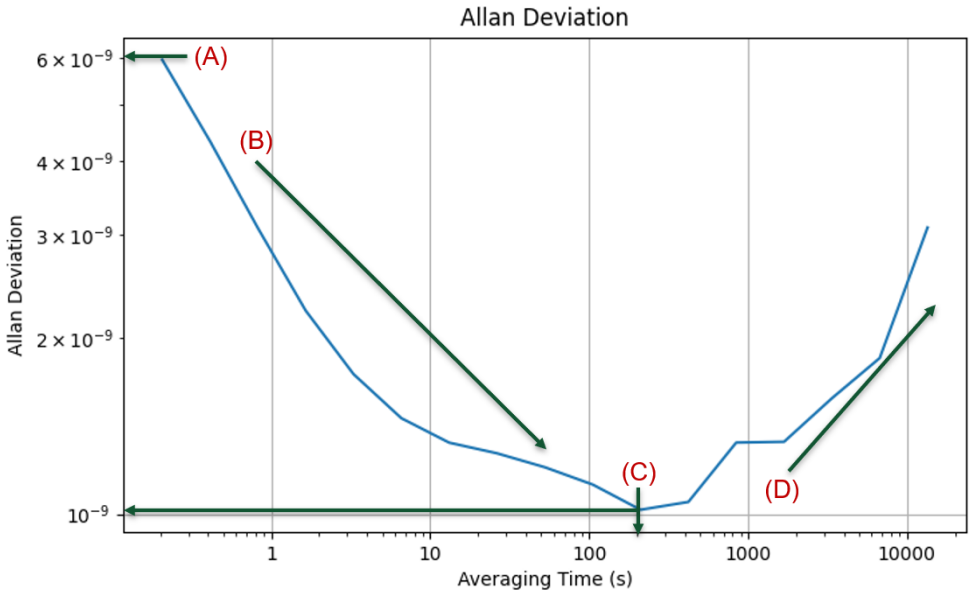

Figure 14: Allan deviation plot example, depicting different points of interest.

Figure 15 portrays the behaviour of the Allan deviation over a duration of 10,000 seconds for both the green (QDLASER QLD0593) and red (Eblana Photonics EP689-0-DM SERIES) lasers. For the green laser, the Allan deviation exhibits a minimum value of 2.30×10^{-10}, occurring at 1.76×10^{3} seconds, and a maximum value of 3.19×10^{-9}. On the other hand, the red laser demonstrates a minimum Allan deviation of 2.14×10^{-9}, occurring at 2.20×10^{2} seconds, with a maximum value of 6.33×10^{-9}.

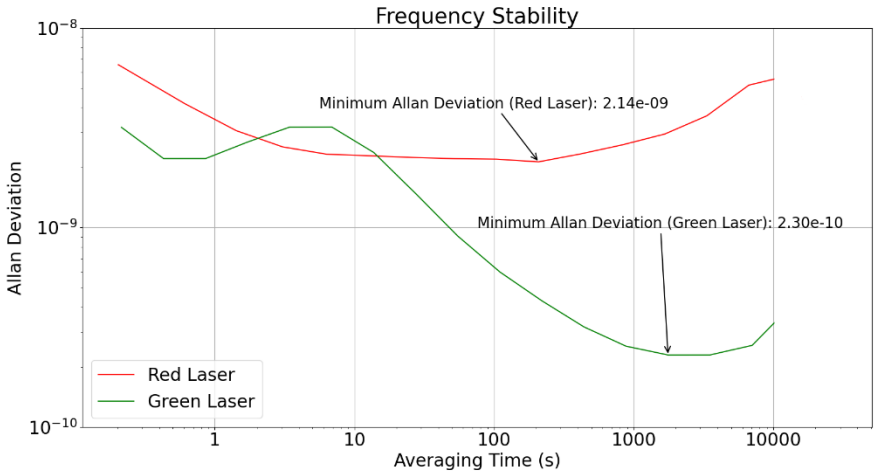

Figure 15: Allan deviation of the green and red lasers over a 10,000-second duration following successful locking.

The noise associated with each data point is represented by the maximum Allan deviation value, which for the green laser is 3.19×10^{-9}. Consequently, an increase in the Allan deviation is observed, which is attributed to the laser temperature stabilizing and introducing noise into the system. Conversely, the red laser exhibits a higher maximum Allan deviation, 6.33×10^{-9}, indicating that the green laser has a lower noise level for each data point.

As data is collected and averaged for both lasers, the Allan deviation decreases, leading to improved data corrections. The green laser reaches its best-case bias after approximately 1.76×10^3 seconds (29 minutes), while the red laser achieves the same point in just 2.20×10^2 seconds (less than 4 minutes). This suggests that the red laser reaches thermal stability at least an order of magnitude faster than the green laser, likely due to differences in their respective heat control mechanisms. Specifically, the green laser employs an external micro-Peltier device for temperature control, while the red laser features an integrated temperature controller within its package, potentially facilitating quicker thermal stability.

The best-case bias, theoretically representing the optimal error level for the sensor, is challenging to achieve in practice. At this minimal bias point, the green laser exhibits an Allan deviation of 2.30×10^{-10}, and the red laser displays a value of 2.14×10^{-9}.

Feature	Green Laser Value	Red Laser Value
Minimum Allan Deviation	2.30×10^{-10}	2.14×10^{-9}
Time at which Minimum Allan Deviation Occurs	$1.76 \times 10^3\ s$	$2.20 \times 10^2\ s$
Maximum Allan Deviation	3.19×10^{-9}	6.33×10^{-9}

Table 3: Allan deviation features and values.

The increase in values observed after reaching the best-case bias can be attributed to low-frequency noise components, such as random walk noise. Although the numerical change in this noise may seem small for a small group of data points, it becomes more pronounced as more data is accumulated. Such low-frequency noise results from the cumulative effect of various factors, including temperature fluctuations, vibrational noise, and random walk.

While true random walk noise eventually averages out to zero over an extended period, comprehensive data collection over a significantly long duration is necessary to capture random walk noise at any reasonable repeat frequency adequately. This approach ensures the appropriate consideration of all relevant random walk noise components during data analysis.

Our laser system demonstrates remarkable frequency stability, with the green laser exhibiting a stability level of 10^{-10} and a frequency uncertainty of 10^{-9}, while the red laser displays a stability level of 10^{-9} and a frequency uncertainty of 10^{-9}. These results exceed the minimum requirements by at least one order of magnitude, making them highly suitable for gauge block interferometry applications.

Although the device was developed in a laboratory with a temperature of $19.9°C \pm 0.2°C$, it is conceivable that the device can operate at different room temperatures (the typical laboratory temperature ranges from $20°C - 25\,°C$). Furthermore, the device seems stable even when the room temperature changes. For instance, all the measurements were taken from an optical test bench, with no protection from air turbulence.

To enhance the system further, several improvements can be implemented. Encasing the setup in an acrylic box would not only facilitate easier transportation but also enhance thermal stability by shielding the system from external temperature fluctuations. Additionally, enclosing the setup in a box would eliminate turbulence caused by the surrounding air, further improving the overall system performance.

It is worth mentioning that during the last weeks of the project a setup where the iodine cell was thermally controlled was build, this approach did not yield any improvements over the laser stability.

4. Conclusion

In this study, we focused on achieving stable laser performance through the use of iodine gas cell, the green and red lasers, with an iodine absorption line. Our aim was to investigate and optimize the stability of these lasers using interferometric techniques and frequency stabilization methods. The results presented here provide valuable insights into the performance characteristics of the lasers and their stability under various conditions.

Frequency stability analysis revealed that both the green and red lasers exhibited remarkable stability levels. The green laser demonstrated an average frequency of $563.815665\,THz$ ($531.720697\,nm$) with an uncertainty of $3\,MHz$ ($2\,fm$), indicating stability on the order of 10^{-9}. The red laser, after careful tuning of its modulation code, achieved an average frequency of $435.377557\,THz$ ($688.580413\,nm$) with an uncertainty of $3\,MHz$ ($4\,fm$), showing a similar level of stability in the range of 10^{-9}. Notably, both lasers maintained their locked state to the corresponding iodine absorption lines for extended durations, confirming the efficacy of the synchronization techniques used.

The Allan deviation analysis provided deeper insights into the noise characteristics and stability of the lasers over time. Both lasers exhibited decreasing Allan deviations as data was averaged, reaching minimal points. The green laser achieved its best-case bias with an Allan deviation of 2.30×10^{-10} at approximately 1.76×10^{3} seconds, while the red laser achieved a slightly higher value of 1.87×10^{-9} at approximately 2.20×10^{2} seconds. This indicated that the red laser achieved thermal stability at least an order of magnitude faster than the green laser, which can be attributed to differences in their heat control mechanisms.

The observed increase in Allan deviation after reaching the best-case bias was attributed to low-frequency noise components, including random walk noise. Comprehensive data collection over extended durations allowed us to capture and account for these noise components accurately.

This master's thesis successfully investigated and optimized the stability of green and red lasers by synchronizing them with an iodine absorption line. The achieved stability levels of around 10^{-9} demonstrate the efficacy of the applied interferometric techniques and frequency stabilization methods. The results contribute to the field of laser technology and interferometry, offering valuable insights into laser stability characteristics and their potential applications.

While this research has provided significant advancements in our understanding of laser stabilization, there are opportunities for further investigations. Future research could explore additional modulation techniques and temperature control mechanisms to enhance laser stability further. Additionally, extending the data collection period for the Allan deviation analysis could provide more comprehensive insights into the long-term noise characteristics of the lasers.

Overall, this study lays a strong foundation for future advancements in laser stabilization and paves the way for the utilization of these stable lasers in various scientific and technological applications.

5. Future Work

While this master's thesis has made significant progress in achieving stable laser performance through synchronization with iodine absorption lines, there are several avenues for future research and improvements in laser stabilization techniques. The following are some potential areas for future work:

Integrated Temperature Control: The impact of different temperature control mechanisms on laser stability can be studied in detail. Integrating temperature control systems directly into the laser package, similar to the red laser, may enhance thermal stability and reduce the time required to reach optimal stability. Comparative studies of various temperature control approaches could shed light on the most effective techniques for different laser types.

Noise Characterization and Mitigation: Extensive noise characterization and mitigation studies can be conducted to identify and address specific noise sources affecting laser stability. Understanding the origins of noise components, including random walk noise, temperature fluctuations, and vibrational noise, will help in developing targeted solutions to minimize their impact on laser performance.

Long-Term Stability Analysis: Extending the duration of Allan deviation analysis beyond the current timeframe could offer valuable insights into the long-term stability of the lasers. Investigating laser stability over days, weeks, or even months could help identify trends and reveal any potential drifts or gradual changes in stability.

Environmental Control: Implementing more rigorous environmental control measures could further improve laser stability. Advanced vibration isolation techniques, active temperature regulation, and shielded enclosures could be employed to minimize the influence of external factors on laser performance.

Dual-Frequency Stabilization: Exploring the possibility of dual-frequency stabilization, where multiple lasers outputting at the same wavelength are stabilized to the same iodine absorption line, could have potential benefits. Dual-frequency stabilization may offer increased redundancy and improve the overall stability and reliability of laser systems.

Applications of Stable Lasers: Investigating and identifying potential applications for the stabilized lasers is an important area of future work. These stable lasers can find applications in precision metrology, optical frequency standards, spectroscopy, and other fields that demand high stability and accuracy.

By addressing these future research areas, the field of laser technology and interferometry can continue to advance, leading to the development of more robust and stable laser systems. The knowledge gained from these investigations can contribute to the improvement of laser-based technologies, fostering innovations in scientific research and practical applications.

6. References

[1] B. J. Bloom, T. L. Nicholson, J. R. Williams, S. L. Campbell, M. Bishof, X. Zhang, W. Zhang, S. L. Bromley and J. Ye, "An optical lattice clock with accuracy and stability at the 10−18 level," *Nature,* no. 506, pp. 71-75, 2014.

[2] T. L. Nicholson, S. L. Campbell, R. B. Hutson, G. E. Marti, B. J. Bloom, R. L. McNally, W. Zhang, M. D. Barrett, M. S. Safronova, G. F. Strouse, W. L. Tew and J. Ye, "Systematic evaluation of an atomic clock at 2 × 10−18 total uncertainty," *Nat. Commun,* vol. 6896, 2015.

[3] I. Ushijima, M. Takamoto, M. Das, T. Ohkubo and H. Katori, "Cryogenic optical lattice clocks," *Nat. Photonics,* no. 6, pp. 185-189, 2015.

[4] E. J. Zang, J. P. Cao, Y. Li, C. Y. Li, Y. K. Deng and C. Q. Gao, "Realization of four-pass I2 absorption cell in 532-nm optical frequency standard," *IEEE Trans. Instrum. Meas.,* no. 56, pp. 673-676, 2007.

[5] Hall, M. L. Eickhoff and J. L., "Optical frequency standard at 532 nm," *IEEE Trans. Instrum. Meas.,* no. 44, pp. 155-158, 1995.

[6] F. Hong, J. Ishikawa, Y. Zhang, R. X. Guo, A. Onae and H. Matsumoto, "Frequency reproducibility of an iodine-stabilized Nd:YAG laser at 532 nm," *Opt. Commun.,* no. 235, pp. 377-385, 2004.

[7] J. L. Hall, L.-S. Ma, M. Taubman, B. Tiemann, F.-L. Hong, O. Pfister and J. Ye, "Stabilization and frequency measurement of the I2-stabilized Nd:YAG laser," *IEEE Trans. Instrum. Meas.,* no. 48, pp. 583-586, 1999.

[8] S. Takemoto, A. Araya, J. Akamatsu, W. Morii, H. Momose, M. Ohashi, I. Kawasaki, T. Higashi, Y. Fukuda, S. Miyoki, T. Uchiyama, D. Tatsumi, H. Hanada, I. Naito, S. Telada, N. Ichikawa, K. Onoue and Y. Wada, "A 100 m laser strainmeter system installed in a 1 km deep tunnel at Kamioka, Gifu, Japan," *J. Geodyn,* no. 38, pp. 477-488, 2004.

[9] J. Ye, L. S. Ma and J. L. Hall, "Molecular iodine clock," *Phys. Rev. Lett.,* vol. 270801, no. 87, 2001.

[10] B. Argence, H. Halloin, O. Jeannin, P. Prat, O. Turazza, E. Vismes, G. Auger and E. Plagnol, "Molecular laser stabilization at low frequencies for the LISA mission," *Phys. Rev. D,* vol. 082002, no. 81, 2010.

[11] M. Takamoto, F.-L. Hong, R. Higashi and H. Katori, "An optical lattice clock," *Nature,* no. 435, pp. 321-324, 2002.

[12] W. Kokuyama, K. Numata and J. Camp, “Simple iodine reference at 1064 nm for absolute laser frequency determination in space applications,” *Appl. Opt.,* no. 2010, pp. 6264-6267, 2010.

[13] F. Hong, M. Takamoto, R. Higashi, Y. Fukuyama, J. Jiang and H. Katori, “Frequency measurement of a Sr lattice clock using an SI-second-referenced optical frequency comb linked by a global positioning system (GPS),” *Opt. Express,* no. 13, pp. 5253-5262, 2005.

[14] M. Musha, T. Kanaya, K. Nakagawa and K. Ueda, “The short- and long-term frequency stabilization of an injection-locked Nd:YAG laser in reference to a Fabry-Perot cavity and an iodine saturated absorption line,” *Opt. Commun.,* no. 183, pp. 165-173, 2000.

[15] A. Cingöz, D. C. Yost, T. K. Allison, A. Ruehl, M. E. Fermann, I. Hartl and J. Ye, “Direct frequency comb spectroscopy in the extreme ultraviolet,” *Nature,* no. 482, pp. 68-71, 2012.

[16] Y. Bitou, K. Sasaki, S. Iwasaki and F. Hong, “Compact I2-stabilized frequency-doubled Nd:YAG laser for long gauge block interferometer,” *Jpn. J. Appl. Phys.,* no. 42, pp. 2867-2871, 2003.

[17] F. Hong, J. Ishikawa, Z. Y. Bi, J. Zhang, K. Seta, A. Onae, J. Yoda and H. Matsumoto, “Portable I2-stabilized Nd:YAG laser for international comparisons,” *IEEE Trans. Instrum. Meas.,* no. 50, pp. 486-489, 2001.

[18] A. Lurie, P. S. Light, J. Anstie, T. M. Stace, P. C. Abbott, F. Benabid and a. A. N. Luiten, “Saturation spectroscopy of iodine in hollow-core optical fiber,” *Opt. Express,* no. 20, pp. 11906-11917, 2012.

[19] T. Yoshizawa and R. Schodel, “Length and Size,” in *Handbook of Optical Metrology Principles and Applications*, Taylor & Francis Group, 2008, pp. 365-389.

[20] C. Johansson, “Mättsats för precisionsmåttagningen”. Sweden Patent SE 17017 C1 2.5., 1901.

[21] “Kösters W,” *Feinmechanik,* no. 1, pp. 39-41, 1922.

[22] J. Barnes and M. Puttock, “National physical laboratory interfeormer,” *Engineer,* no. 196, pp. 763-766, 1953.

[23] A. Twyman and F. Green, “Improvements in finishing”. British Patent 103832, 1916.

[24] “Documents concerning the new definition of the metre,” *Metrologia,* no. 19, pp. 163-177, 1984.

[25] G. Bönsch, “Automatic gauge block measurement by phase stepping interferometry with three laser wavelengths,” *Proc. SPIE,* no. 4401, pp. 1-10, 2001.

[26] K. Pugh and Jackson, “Automatic gauge block measurement using multiple wavelength interferometry,” *Proc. SPIE,* no. 656, pp. 244-250, 1986.

[27] T. Hariharan, B. Oreb and Eiju, “Digital phase-shifting interferometry: a simple error-compensating phase calculation algorithm,” *Appl. Opt.,* no. 26, pp. 2504-2505, 1987.

[28] G. Bönsch and Böhme, “Phase-determination of Fizeau interferences by phase-shifting interferometry,” *Optik,* no. 83, pp. 161-164, 1989.

[29] P. Carré, “Installation et utilisation du comparateur photoélectrique et interférentiel du Bureau International des Poids et Measures,” *Metrologia,* no. 2, pp. 13-23, 1966.

[30] M. Servin, M. Q. J. A and Padilla, “The general theory of phase shifting algorithms,” *Opt. Express,* no. 17, pp. 21867-21881, 2009.

[31] M. Servin, M. Q. A and Padilla, “Fringe Pattern Analysis for Optical Metrology: Theory, Algorithms, and Applications,” *Weinheim: Wiley-VCH,* 2014.

[32] M. A. V. Zeeland, T. N. Carlstrom, D. K. Finkenthal, R. L. Boivin, A. Colio, D. Du, A. Gattuso, F. Glass, C. M. Muscatello and R. O'Neill, Tests of a two-color interferometer and polarimeter for ITER density measurements, vol. 59, IOP Publishing Ltd, 2017.

[33] H. Kang, B. J. Chun, Y.-S. Jang, Y. Kim and S. Kim, “Real-time compensation of the refractive index of air in distance measurement,” *Opt. Express,* vol. 23, pp. 26377-26385, 2015.

[34] F. Krause, E. Benkler, C. Nölleke, P. Leisching and U. Sterr, “Simple and compact diode laser system stabilized to Doppler-broadened iodine lines at 633 nm,” *Appl. Opt.,* vol. 59, pp. 10808-10812, 2020.

[35] S. Gerstenkorn and P. Luc, Atlas du spectre d’absorption de molécule d’iode, Laboratoire Aimé Cotton, 1978.

[36] HighFinesse, “Description of the Wavelength Meter WS-7-30,” HighFinesse, [Online]. Available: https://www.highfinesse.com/en/wavelengthmeter/wavelengthmeter-ws-7-60.html. [Accessed 10 06 2023].

[37] C. Nölleke, P. Leisching, G. Blume, D. Jedrzejczyk, J. Pohl, D. Feise, A. Sahm and K. Paschke, “Frequency locking of compact laser-diode modules at 633 nm,”

International Society for Optics and Photonics (SPIE), vol. 10539, p. 28–33, 2018.

[38] J. W. Tukey, "Exploratory Data Analysis," *Addison-Wesley,* 1977.

[39] M. Hubert and E. Vandervieren, "An adjust boxplot for skewed distributions," *Computational Statistics and Data Analysis,* vol. 12, no. 55, pp. 5186-5201, 2008.

[40] W. Riley, Handbook of Frequency Stability Analysis, NIST, 2028.

[41] D. F. Riehle, Frequency Standards: Basics and Applications, Wiley-VCH Verlag GmbH & Co. KGaA, Weinheim, 2003.

[42] J. Walls and F. Rutman, "Characterization of frequency stability in precision frequency sources,," *Proceedings of the IEEE,* vol. 79, pp. 952-960, 1991.

[43] D.A.Howe, D.W.Allanand and J.A.Barnes, "PropertiesofSignalSources andMeasurementMethods," *Proceedings of the 35th Annual Symposium on Frequency Control,* 1981.

[44] F. Krause, E. Benkler, C. Nölleke, P. Leisching and U. Sterr, "Simple and compact diode laser system stabilized to Doppler-broadened iodine-lines at 633 nm," *Optica,* no. 59, pp. 10808-10812, 2020.

[45] Y. H. Chen, W. C. Lin, J. T. Shy and H. C. Chui, "Iodine-stabilizedsingle-frequencygreen InGaNdiodelaser," *Optics Letters,* vol. 43, no. 1, 2017.

[46] A. E. Wallin, D. Price, C. G. Carson, F. Meynadier, Y. Xie and E. Benkler, "AllanTools 2019.9," 20 September 2019. [Online]. Available: https://pypi.org/project/AllanTools/. [Accessed 2023 July 26].

Appendix

Python Acquisition Code

```
import serial
import csv
from datetime import datetime
ser = serial.Serial('COM6', 9600) # Replace 'COM6' with the port name
of your microcontroller
with open('C:\\Users\\RFRUBEN\\OneDrive - Teknologian Tutkimuskeskus
VTT\\Documents\\csv\\data.csv', 'w', newline='') as csvfile:
    writer = csv.writer(csvfile)
    while True:
        data = ser.readline().decode('utf-8') # Decode the byte string
        values = data.strip().split(' ')
        values = [float(v) for v in values]
        now = datetime.now()
        timestamp = now.strftime("%Y-%m-%d %H:%M:%S.%f")
        writer.writerow([timestamp] + values)
        print([timestamp] + values)
```

MATLAB Code

```
clear;

% read csv file
data    =    readtable('C:\Users\RFRUBEN\OneDrive    -    Teknologian
Tutkimuskeskus   VTT\Documents\csv\24.07.2023,   10.02,     435,322074
THz.csv', 'Delimiter', '\t'); % temperature red

% Remove first two rows
data(1:2,:) = [];

% Replace commas with decimal points
data{:,1:2} = replace(data{:,1:2}, ',', '.');

% Convert cell arrays to numeric arrays
wavelength = cellfun(@str2double, data{:,2});
time = cellfun(@str2double, data{:,1});

% Remove the third column
data(:, 3) = [];

% Convert time values to seconds
time = time / 1000; % Convert time to seconds
% time = time / 36000000; % Convert time to hours

figure(6)
plot(time, wavelength)

% Filter data for the desired range of seconds
time_range_start = 0;
time_range_end = 100000;
```

```
% Find the indices of the time values within the specified range
indices = (time >= time_range_start) & (time <= time_range_end);

% Apply the indices to select the corresponding time and wavelength
values
time_filtered = time(indices);
wavelength_filtered = wavelength(indices);

% Calculate the lower and upper bounds using IQR method on the filtered
data
Q1 = prctile(wavelength_filtered, 25);
Q3 = prctile(wavelength_filtered, 75);
IQR = Q3 - Q1;
lower_bound = Q1 - 1.5 * IQR;
upper_bound = Q3 + 1.5 * IQR;

% Remove outliers
outlier_mask    =    (wavelength_filtered    >=    lower_bound)    &
(wavelength_filtered <= upper_bound);
wavelength_filtered = wavelength_filtered(outlier_mask);
time_filtered = time_filtered(outlier_mask);

figure(4)
plot(time_filtered, wavelength_filtered);

% Wavenumber
wave_num_filtered = (1 ./ wavelength_filtered) * 10000000;

% Frequency
freq_filtered = (299792458 * 10^9 * 10^-12) ./ wavelength_filtered;

% Calculate the average and standard deviation of the filtered data
average_wavelength = mean(wavelength_filtered);
standard_deviation_wavelength = std(wavelength_filtered);

average_wave_num = mean(wave_num_filtered);
standard_deviation_wave_num = std(wave_num_filtered);

average_freq = mean(freq_filtered);
standard_deviation_freq = std(freq_filtered);

figure(1)
plot(time_filtered, wavelength_filtered);

% Plot the average as a horizontal line
hold on;
plot([time_filtered(1)    time_filtered(end)],    [average_wavelength
average_wavelength], 'r--', 'LineWidth', 2);

% Plot vertical lines to represent the standard deviation
plot([time_filtered(1)  time_filtered(end)],  [average_wavelength  +
standard_deviation_wavelength          average_wavelength          +
standard_deviation_wavelength], 'k--', 'LineWidth', 1);
```

```
plot([time_filtered(1)  time_filtered(end)],  [average_wavelength  -
standard_deviation_wavelength          average_wavelength          -
standard_deviation_wavelength], 'k--', 'LineWidth', 1);

xlabel('Seconds');
ylabel('Wavelength (nm)');
legend('Data',  ['Average  =  '  num2str(average_wavelength)  '  nm'],
['Standard Deviation = ' num2str(standard_deviation_wavelength * 10^6)
' fm']);
title('Wavelength');

figure(2)
plot(time_filtered, wave_num_filtered);

% Plot the average as a horizontal line
hold on;
plot([time_filtered(1)     time_filtered(end)],     [average_wave_num
average_wave_num], 'r--', 'LineWidth', 2);

% Plot vertical lines to represent the standard deviation
plot([time_filtered(1)   time_filtered(end)],   [average_wave_num   +
standard_deviation_wave_num            average_wave_num            +
standard_deviation_wave_num], 'k--', 'LineWidth', 1);
plot([time_filtered(1)   time_filtered(end)],   [average_wave_num   -
standard_deviation_wave_num            average_wave_num            -
standard_deviation_wave_num], 'k--', 'LineWidth', 1);

xlabel('Seconds');
ylabel('Wavenumber (1/cm)');
legend('Data',  ['Average  =  '  num2str(average_wave_num)  '  1/cm'],
['Standard  Deviation  =  '  num2str(standard_deviation_wave_num)  '
1/cm']);
title('Wavenumber');

figure(3)
plot(time_filtered, freq_filtered);

% Plot the average as a horizontal line
hold on;
plot([time_filtered(1)       time_filtered(end)],       [average_freq
average_freq], 'r--', 'LineWidth', 2);

% Plot vertical lines to represent the standard deviation
plot([time_filtered(1)    time_filtered(end)],    [average_freq    +
standard_deviation_freq average_freq + standard_deviation_freq], 'k--
', 'LineWidth', 1);
plot([time_filtered(1)    time_filtered(end)],    [average_freq    -
standard_deviation_freq average_freq - standard_deviation_freq], 'k--
', 'LineWidth', 1);

xlabel('Time [s]', 'FontSize', 24);
ylabel('Frequency (THz)', 'FontSize', 24);
legend('Data', ['Average = ' sprintf('%.6g', average_freq) ' THz' ' =
' sprintf('%.6g', average_wavelength) ' nm'], ['Standard Deviation = '
```

```
sprintf('%.1g', standard_deviation_freq * 10^6) ' MHz' ' = '
sprintf('%.1g', standard_deviation_wavelength * 10^6) ' fm'],
'FontSize', 24);
title('Frequency Stability', 'FontSize', 30);
set(gca, 'FontSize', 24); % Increase font size of tick labels

% Plot the frequency distribution
figure(5)
histogram(freq_filtered, 'Normalization', 'probability');
hold on;
xline(average_freq, 'r--', 'LineWidth', 2);
xlabel('Frequency (THz)', 'FontSize', 24);
ylabel('Probability', 'FontSize', 24);
legend('Frequency Distribution', ['Average = ' sprintf('%.6g',
average_freq) ' THz' ' = ' sprintf('%.6g', average_wavelength) ' nm'],
'FontSize', 24);
title('Frequency Distribution', 'FontSize', 30);
set(gca, 'FontSize', 24); % Increase font size of tick labels
```

Allan Calculation Python Code

```
import pandas as pd
import numpy as np
import matplotlib.pyplot as plt
from matplotlib.ticker import ScalarFormatter
import allantools

plt.rcParams.update({'font.size': 24})

# Read CSV file, skipping the first 57 rows
data = pd.read_csv('C://Users//RFRUBEN//OneDrive - Teknologian
Tutkimuskeskus VTT//Documents//csv//15.05.2023.csv', delimiter='\t',
skiprows=57) # Green laser

# Replace commas with decimal points
data.replace(',', '.', regex=True, inplace=True)

# Convert cell arrays to numeric arrays
wavelength = data.iloc[:, 1].astype(float).to_numpy()
time = data.iloc[:, 0].astype(float).to_numpy() / 1000  # Convert time
to seconds

# Prompt the user to input the desired time range
start_time = float(input("Enter the start time (in seconds): "))
end_time = float(input("Enter the end time (in seconds): "))

# Filter data within the specified time range
time_mask = (time >= start_time) & (time <= end_time)
wavelength_filtered = wavelength[time_mask]
time_filtered = time[time_mask]


# Calculate the average of the wavelength data
wavelength_average = np.mean(wavelength_filtered)
```

```
wavelength_nor = wavelength_filtered / wavelength_average

# Calculate the time interval between consecutive data points
time_interval = np.diff(time_filtered)

# Calculate the average sampling rate
average_rate = 1 / np.mean(time_interval)
print(average_rate)

# Calculate the Allan deviation
taus, adevs, _, _ = allantools.adev(wavelength_nor, data_type="freq",
rate=average_rate)

# Find the minimum Allan deviation and its corresponding tau value
min_adev = np.min(adevs)
min_adev_tau = taus[np.argmin(adevs)]

# Calculate the standard deviation of the wavelength_filtered data
wavelength_std = np.std(wavelength_filtered)

# Find the maximum Allan deviation and its corresponding tau value
max_adev = np.max(adevs)
max_adev_tau = taus[np.argmax(adevs)]

print(f'Standard      Deviation      of      Wavelength      Filtered:
{wavelength_std:.2e}')
print(f'Highest   Allan   Deviation:   {max_adev:.2e}   at   tau   =
{max_adev_tau:.2e}')
print(f'Minimum   Allan   Deviation:   {min_adev:.2e}   at   tau   =
{min_adev_tau:.2e}')

# Read CSV file for data1, skipping the first 57 rows
data1   =   pd.read_csv('C://Users//RFRUBEN//OneDrive   -   Teknologian
Tutkimuskeskus  VTT//Documents//csv//24.07.2023,  10.02,    435,322074
THz.csv', delimiter='\t', skiprows=57) # Red laser

# Replace commas with decimal points for data1
data1.replace(',', '.', regex=True, inplace=True)

# Convert cell arrays to numeric arrays for data1
wavelength1 = data1.iloc[:, 1].astype(float).to_numpy()
time1 = data1.iloc[:, 0].astype(float).to_numpy() / 1000   # Convert
time to seconds

# Filter data1 within the specified time range
time_mask1 = (time1 >= start_time) & (time1 <= end_time)
wavelength_filtered1 = wavelength1[time_mask1]
time_filtered1 = time1[time_mask1]

# Calculate the average of the filtered wavelength data for data1
wavelength_average1 = np.mean(wavelength_filtered1)

wavelength_nor1 = wavelength_filtered1 / wavelength_average1
```

```
# Calculate the time interval between consecutive data points for data1
time_interval1 = np.diff(time_filtered1)

# Calculate the average sampling rate for data1
average_rate1 = 1 / np.mean(time_interval1)
print(average_rate1)

# Calculate the Allan deviation for data1
taus1,    adevs1,    _,    _    =    allantools.adev(wavelength_nor1,
data_type="freq", rate=average_rate1)

# Find the minimum Allan deviation and its corresponding tau value for
data1
min_adev1 = np.min(adevs1)
min_adev_tau1 = taus1[np.argmin(adevs1)]

# Find the maximum Allan deviation and its corresponding tau value for
data1
max_adev1 = np.max(adevs1)
max_adev_tau1 = taus1[np.argmax(adevs1)]

print(f'Standard   Deviation   of   Wavelength   Filtered   (data1):
{wavelength_std:.2e}')
print(f'Highest  Allan  Deviation  (data1):  {max_adev1:.2e}  at  tau  =
{max_adev_tau1:.2e}')
print(f'Minimum  Allan  Deviation  (data1):  {min_adev1:.2e}  at  tau  =
{min_adev_tau1:.2e}')

# Plot the Allan deviation for data1
fig, ax = plt.subplots()
ax.loglog(taus1, adevs1, label='Red Laser', color='red')  # Plot for
data1
ax.loglog(taus, adevs, label='Green Laser', color='green')  # Plot for
data
ax.set_ylim(1e-10, 1e-8)
ax.set_xlabel('Averaging Time (s)')
ax.set_ylabel('Allan Deviation')
ax.set_title('Frequency Stability')
ax.grid(True)
ax.legend()

# Set the x-axis tick label formatter to ScalarFormatter
ax.xaxis.set_major_formatter(ScalarFormatter())

# Annotate the lowest point on the plot for data1
ax.annotate(f'Minimum Allan Deviation (Red Laser): {min_adev1:.2e}',
xy=(min_adev_tau1, min_adev1), xycoords='data',
            xytext=(0.3, 0.8), textcoords='axes fraction',
            arrowprops=dict(arrowstyle="->", lw=1.5, color='black'),
            fontsize=20, color='black')

# Annotate the lowest point on the plot for data
```

```
ax.annotate(f'Minimum Allan Deviation (Green Laser): {min_adev:.2e}',
xy=(min_adev_tau, min_adev), xycoords='data',
            xytext=(0.5, 0.5), textcoords='axes fraction',
            arrowprops=dict(arrowstyle="->", lw=1.5, color='black'),
            fontsize=20, color='black')

plt.show()
```